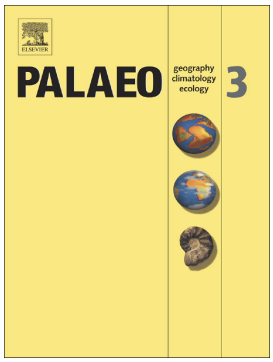

Magnetostratigraphy of the Punta Grohmann section (Dolomites, Italy): improving the chronology of the Ladinian/Carnian boundary

Matteo Maron, Giovanni Muttoni, Paolo Mietto, Piero Gianolla

PII: S0031-0182(24)00066-X

DOI: https://doi.org/10.1016/j.palaeo.2024.112077

Reference: PALAEO 112077

To appear in: *Palaeogeography, Palaeoclimatology, Palaeoecology*

Received date: 6 May 2023

Revised date: 1 February 2024

Accepted date: 2 February 2024

Please cite this article as: M. Maron, G. Muttoni, P. Mietto, et al., Magnetostratigraphy of the Punta Grohmann section (Dolomites, Italy): improving the chronology of the Ladinian/Carnian boundary, *Palaeogeography, Palaeoclimatology, Palaeoecology* (2024), https://doi.org/10.1016/j.palaeo.2024.112077

MAGNETOSTRATIGRAPHY OF THE PUNTA GROHMANN SECTION (DOLOMITES, ITALY): IMPROVING THE CHRONOLOGY OF THE LADINIAN/CARNIAN BOUNDARY

Matteo Maron[1], Giovanni Muttoni[2], Paolo Mietto[3], Piero Gianolla[4]

[1]*Department of Engineering and Geology, University "G. D'Annunzio" of Chieti-Pescara, Via dei Vestini 31, 66100 – Chieti, Italy. E-mail: matteo.maron@unich.it*

[2]*Department of Earth Sciences "Ardito Desio", University of Milano, via Mangiagalli 34, 20133 – Milano, Italy.*

[3]*Department of Geosciences, University of Padova, via Gradenigo 6, 35131-Padova, Italy.*

[4]*Department of Physics and Earth Sciences, University of Ferrara, via Saragat 1, 44122 – Ferrara, Italy.*

Keywords: Triassic; paleomagnetism; GPTS

Abstract

We provide the magnetostratigraphy of the Ladinian/Carnian Punta Grohmann stratigraphic section (Dolomites, Italy), calibrated with U-Pb ages from the literature (237.58 ± 0.04 Ma; 237.68 ± 0.05 Ma). The FO of ammonoid *Zestoceras lorigae,* the base of the vigens-densus palynomorphs Zone, and sequence stratigraphy suggest a Carnian age for the upper part of the section, which has been confirmed by the magnetostratigraphic correlation between Punta Grohmann and Prati di Stuores (Carnian GSSP). Additional magnetostratigraphic correlation between Punta Grohmann and key time-calibrated Ladinian–Carnian sections from the literature (e.g., Mayerling, Seceda, Rio Nigra)

lead to a more precise age of the Carnian base (~236.5 Ma) and to a better definition of the Middle–Late Triassic Geomagnetic Polarity Time Scale.

1. Introduction

The Ladinian/Carnian boundary is formally placed in bed SW4 of the Prati di Stuores global stratigraphic section and point (GSSP) (San Cassiano Formation; Mietto et al., 2012) at the first appearance datum (FAD) of ammonoid *Daxatina canadensis* (Whiteaves, 1889), while the FAD of conodont *Paragondolella polygnathiformis* (Budurov and Stefanov, 1965) represents a secondary marker (Broglio Loriga et al., 1999; Mietto et al., 2008; Mietto et al., 2012). The Ladinian in the Dolomites of northern Italy is characterized by intense volcanic activity lasting at least ~5 Myr (Storck et al., 2019). The chronology of the Ladinian of the Dolomites mainly relies on radiometric U-Pb ages from the Buchenstein Formation (Fm.) at Seceda (Wotzlaw et al., 2018) and from the Frommer member (mb.) of the Fernazza Fm. at Rio Nigra (Mietto et al., 2012; Maron et al., 2019; Gianolla et al., 2021). Although both sections are accompanied by magneto- and biostratigraphic data, they do not cover the entire Ladinian, making the chronology of this Stage still open to refinement. The age of the Ladinian/Carnian boundary has been approximated at ca. 237 Ma considering the radiometric (U-Pb) age of 237.77±0.14 Ma obtained from Rio Nigra (Mietto et al., 2012; Maron et al., 2019) and estimating the sedimentation rates of the in-between basinal formations up to the basal Carnian level. Recently, Maron et al. (2019) proposed a similar age of ca. 236.8 Ma for the base of the Carnian derived from the compilation of an updated Geomagnetic Polarity Time Scale (GPTS) for the Triassic that used the same radiometric age from Rio Nigra as a chronological tie-point.

Here, we attempt to further refine the chronology of the Carnian Stage by investigating the magnetostratigraphy and biostratigraphy of the Ladinian–Carnian marine section of Punta Grohmann (Dolomites, Italy). This section is well calibrated by two radiometric U-Pb datings on zircons (237.58±0.04 Ma, 237.68±0.05 Ma; Storck et al., 2019) and is accompanied by ammonoid,

conodont and palynomorphs biostratigraphy (Van der Eem, 1983; Russo et al., 1997; Gianolla et al., 1998; Mietto et al., 2008). The Punta Grohmann section has also been studied for sequence stratigraphy, where the Car-1 3rd order cycle (Gianolla et al., 1998) represents most of the section (Mietto et al., 2012; Gianolla et al., 2021).

2. Geological Setting

2.1 Lithostratigraphy

Punta Grohmann is a classic upper Ladinian-lower Carnian basinal section (Ogilvie-Gordon, 1927; Scudeler Baccelle, 1974; Russo et al., 1997; Gianolla et al., 1998, 2021) outcropping at the base of the Sassolungo/Langkofel Massif, 1.5 km to the west of Passo Sella and 20 km from the village of Canazei in the Dolomites (Italy) (Fig. 1A).

The Punta Grohmann section is a ca. 570 m-thick sequence of basinal siliciclastic (mainly volcaniclastic) and carbonatic deposits belonging to the Wengen Fm. and San Cassiano Fm. (Figs. 1B, 2B, 3A). The section lies above a chaotic assemblage (Caotico Eterogeneo *Auct.*) with large blocks of pre-volcanic rocks (mainly from Anisian-Ladinian carbonates and Lower Triassic Werfen Fm. siliciclastics) embedded in a volcaniclastic matrix, followed by tens to hundreds of meters (~300-400 m; Storck et al., 2019) of volcanites (pillow lavas, pillow breccias, hyaloclastites) belonging to the Fernazza Fm (Bosellini et al., 1982, Castellarin et al., 1998; Brandner & Keim, 2011; Gianolla et al., 2021) (Fig. 1B). The base of the section is marked by a submarine erosional surface overlain by the Marmolada Conglomerate (Cgm.), which is the basal facies of the Wengen Fm. characterized by para-conglomerates with well-rounded lava pebbles followed by mass flow and channelized high density turbidites and massive dark-colored sandstones (De Zanche and Gianolla, 1995; Russo et al., 1997; Gianolla et al., 1998, 2021) (Fig. 2A). The Marmolada Cgm. is overlain by ca. 150 meters of the typical facies of the Wengen Fm. (thin bedded turbiditic sandstones alternated with dark pelites). In this part of the section rare calcarenitic levels and platform-derived carbonatic material are found, indicating the presence of a nearby active reef

complex. A chaotic assemblage of carbonate olistoliths embedded in the volcaniclastic sediments is found at the top of the turbiditic unit, with blocks up to five meters in size and channelized carbonatic breccias, which are interpreted to indicate erosion of syn- to post-volcanic carbonate platforms or gravitational re-deposition during platforms progradation (Russo et al., 1997). A subsequent decrease in siliciclastic input is documented above the olistolithic interval, with ca. 100 m of volcaniclastic sandstones, pelites, marlstones and thin levels of grey/reddish nodular limestones extending from level ~165 m to ~265 m in the sampled section (Fig. 2A). In this interval, channelized turbidites, slumps, and mud flows are frequent. Thin ash-beds are preserved in the mud-dominated part of the sequence. Two U-Pb radiometric ages (237.579 ± 0.042 Ma; 237.680 ± 0.047 Ma) have been obtained from Isotope Dilution-Thermal Ionization Mass Spectrometry (ID-TIMS) on selected zircons sampled from one of the ash-beds at ca. 220 m (Storck et al., 2019) (Fig. 2A).

The upper part of the section (San Cassiano Fm.) shows a general coarsening-upward trend and an increase in siliciclastic and carbonatic input, the latter derived from prograding carbonate platforms. The initial part of the San Cassiano Fm. is characterized by the presence of slumped deposits, slump scars and channelized turbidites. The terrigenous fraction is represented by shales alternating with reworked volcanic sandstones or hybrid arenites. Carbonates are mainly bio-intraclastic calcarenites rich in coated grains, automicritic clasts, and bioclasts. Ooids are also present (e.g., Stefani et al., 2010). In this interval, there are also isolated calcareous blocks and carbonatic megabreccias derived from the surrounding platforms. In general, carbonatic sediments become more abundant moving upward in the section, because of the interfingering between the San Cassiano Fm. and the Cassian Dolomite (Fig. 1B). The top of the section is characterized by some meters of carbonatic megabreccias of the toe of the slope of the overlying Cassian carbonate platform. The contact with the clinostratified slope of the Cassian Dolomite is disturbed by a minor fault.

The section has been interpreted also in terms of sequence stratigraphy (Gianolla et al., 1998, 2021; Mietto et al., 2012). The sequence boundary (SB, correlative conformity placed at the onset of the

relative sea level fall) is positioned at the erosional contact between the coarse conglomerates (Marmolada Cgm.) and the underlying volcanic and volcaniclastics of the Fernazza Fm. (previous Highstand System Tract – HST deposits). The SB is not represented in the section here considered (Fig. 2A) but lies a few meters below the Marmolada Cgm. (Gianolla et al., 2021). The lower part of the Wengen Fm. is characterized by conglomerates, mass-flow and high-density turbidites representative of the Falling Stage System Tract (FSST), followed by thin bedded low-density turbidites interbedded with dark pelites, volcaniclastic sandstones and conglomerates representing the Lowstand System Tract (LST) (Fig. 2A). Calcarenites and horizons of channelized carbonate breccias and olistolith swarms characterize the regressive interval of LST (Fig. 2A). Above the carbonate olistoliths, a decrease in the siliciclastic supply was accompanied by the deposition of volcaniclastic siltstones, pelites, marlstones and thin beds of grey nodular limestone (Transgressive System Tract – TST). The upper part of the succession is characterized by a general coarsening-upward trend with an increase in the siliciclastic and carbonate supply related to the progradation of the terrigenous and carbonate shelf, representing Highstand System Tract (HST) deposits.

2.2 Biostratigraphy

The biostratigraphic record from the Punta Grohmann section is mainly represented by ammonoids and palynomorph, with reported, but not stratigraphically placed, conodonts (Van der Eem, 1983; Mietto and Manfrin 1995a, Russo et al. 1997, Gianolla et al. 1998, Mietto et al. 2008).

2.2.1 Ammonoids

From the point of view of the ammonoid faunas, the section was illustrated for the first time by Mietto and Manfrin (1995a). New sampling in the upper part of the section allowed a revision of the previous data (Fig. 2B, 3B; Tab. 1). Despite a bed-by-bed study of the section, only about thirty specimens could be collected; the fauna is therefore poorly represented and fragmentary. Specimens

were collected from pelitic and calcarenitic layers. In the calcarenites, the specimens typically appear as internal molds (see Mietto et al., 2008).

Starting from the base of the section, the association of long-ranging species, as *Lecanites glaucus* (Münster, 1834) and *Lobites ellipticus* (Hauer, 1860) associated with *Maclearnoceras* and *Asklepioceras*, can be referred to the lower part of the Regoledanus Subzone.

In beds GRH2a (~190 m), GRH3 (~480 m) and GRO10 (~530 m) (Figs. 2B, 3A, 3B; Tab. 1), we recovered the most significant element of the ammonoid faunas of the Punta Grohmann section, which is *Frankites apertus* (Mojsisovics, 1893) (Fig. 3C). This species has a short range at the Ladinian-Carnian boundary interval, between the upper part of the Regoledanus and the following Canadensis Subzone (*sensu* Mietto and Manfrin, 1995b). Outside the Tethys realm, *F. apertus* is documented also in the Boreal domain (Tozer, 1994) under the synonym *F. sutherlandi* (McLearn, 1947) (Mietto et al., 2008, 2012).

The ammonoids recovered in the interval between the first occurrence of *F. apertus* in bed GRH2a and the first occurrence of *Celtites epolensis* Mojsisovics, 1882 in bed GRH80 (~490 m; Fig. 2A; Tab. 1) are referred to the upper part of the Regoledanus Subzone. The occurrence of the ammonoid *Celtites epolensis*, which has never been found in the Carnian (see Mojsisovics, 1882, Broglio Loriga et al., 1999, Balini et al., 2000), constrains a large part of the Punta Grohmann section, up to ~490 m, to the upper Ladinian. *C. epolensis* is well known from the Wengen Fm. of Lombardy-Giudicarie (*stratum tipicum* and type area for this species, respectively), where it seems confined to the lower part of the upper Ladinian (Balini et al., 2000).

Outside the type area, Mietto et al. (2008) reported *C. epolensis* from 12 additional localities/sections of the Southern Alps (other than Punta Grohmann), where this species covers an upper Ladinian biostratigraphic interval that includes the Neumayri and Regoledanus Subzones, up to the Carnian base (Mietto and Manfrin, 1995a, 1995b).

In one of these sections (Val Giaule 2, Pieve di Cadore, Belluno), the single specimen of *C. epolensis* described in Mietto and Manfrin (1995b: pl. 1, fig. 18) from bed VG 40, and reported also

in Broglio Loriga et al. (1998), shows a shape of the ribs that does not seem to fit perfectly into the original description and illustration of Mojsisovics (1882). In bed VG 40, this specimen was found in association with *Celtites* sp., *Asklepioceras* sp., *Protrachyceras* sp. and *Zestoceras* cf. *enode* (Tozer, 1972), a fauna attributed to the upper Ladinian Regoledanus Subzone (Mietto and Manfrin, 1995b; Mietto et al., 2008).

In any case, the specimen of *C. epolensis* from Punta Grohmann reported in this work is defined according to the original criteria of Mojsisovics (1882), and its co-presence with *F. apertus* indicates a late Ladinian age for the lower and middle part of the Punta Grohmann section.

The Carnian ammonoid *Zestoceras lorigae* (Mietto et al., 2008) is documented near the top of the section, in bed GRO10 (~530 m; Figs. 2B, 3A, 3B), where it is associated with *F. apertus* and a probable new species of *Celtites* (Tab. 1). This latter differs from *Celtites epolensis* in having a different ornamentation, characterized by thinner, thicker and less proverse ribs. Unfortunately, the specimens at our disposal are too fragmentary for a precise diagnosis, therefore we prefer to use for these specimens an open nomenclature (*Celtites* sp. A). The first occurrence of *Zestoceras lorigae* at meter ~530 is here used to approximate the base of the Carnian (base of the Canadensis Subzone; see ammonoid distribution of the Prati di Stuores Carnian GSSP, Mietto et al. 2012).

In a recent sampling campaign, four very significant new specimens, even if fragmentary or poorly preserved, have been identified at Punta Grohmann in beds GRO10 and GRH90.

The first one (GRO-10.5; Fig. 3D) consists of an internal mold of *Carnites* sp. in which the ammonitic suture line is well recognizable. Unfortunately, it was not possible to isolate this specimen from the outcrop.

Other two specimens (GRO-10.7 and GRO-10.8) are attributed to fragments, of internal sides of trachyceratids (Fig. 3E). Both fragments show ribs ornamented with pointed tubercles separated by narrow and deep intercostal spaces, which suggest to assign these specimens to either *Trachyceras* sp. or to *Daxatina* sp. (Fig. 3E). Lack of observable sutural line prevents the discrimination of these

two taxa, which in any case appear both in the basal Carnian Canadensis Subzone as in the Prati di Stuores/Stuores Wiesen GSSP section (Mietto et al 2008, 2012).

Finally, in level GRH90, just below level GRO10, another specimen (GRH-90.1, left in situ) is an almost complete internal side of a test referable to *Asklepioceras* sp. (Fig. 3F), a genus which is documented, not only in the Tethys Realm, from the Regoledanus Subzone (late Ladinian) to Aon Subzone (early Carnian) (or correlative subzones in the Boreal realm).

With the exception of the specimens GRO-10.5 and GRH-90.1 (in situ), all the material is stored at the Geological and Paleontological Museum of the Padova University.

2.2.2 Conodonts

The conodont fauna reported by Russo et al. (1997) is characterized by the presence of *Budurovignathus hungaricus* (Kozur and Vegh, 1972), *B. mungoensis* (Diebel, 1956), *B.* cf. *longobardicus* (Kovacs, 1983), *Gladigondolella tethydis* (Huckriede, 1958), and *Pseudofurnishius murcianus* (van de Boogaard, 1966), species that range from late Ladinian (Longobardian) to the early Carnian (early Julian), but their stratigraphic position within the section has not been clarified by the authors. Unfortunately, the secondary conodont biomarker of the Carnian base, *Paragondolella polygnathiformis* (Budurov and Stevanov, 1965) (Mietto et al., 2008, 2012), has not been found at Punta Grohmann.

2.2.3 Palynomorphs

Regarding the palynostratigraphy, Van der Eem (1983) described at Punta Grohmann a rich palynological association characterized by elements like *Camerosporites secatus* Leschik, 1956 emend. Scheuring, 1970, *Ovalipollis pseudoalatus* Thiergart (Schuurman, 1976), *Partitisporites* spp. and *Cycadopites*. Based on this association, Van der Eem (1983) attributed the middle-lower part of Punta Grohmann section to the Secatus-Dimorphus and Secatus-Vigens phases, which are considered late Ladinian in age. In the upper part of the section, the appearance of *Vallasporites*

ignacii (Leschik, 1956), *Lagenella martinii* (Leschik, 1956; Klaus, 1960) and *Patinasporites densus* Leschik, 1956 emend. Scheuring, 1970 suggests a Carnian age (Vigens-Densus Phase; Fig. 2B). A similar pollen assemblage characterizes the Prati di Stuores/Stuores Wiesen Carnian GSSP (Broglio Loriga, et al., 1999; Mietto et al 2012).

3. Paleomagnetism

3.1 Material and methods

A total of 93 standard (~10 cc) drill core samples have been recovered from the Punta Grohmann section, 31 directly from the outcrop and 62 from oriented hand-picked blocks. Samples have been collected avoiding parts of the section disturbed by slumps (Fig. 3A-B). All samples were thermally demagnetized in steps of 50°C-25°C from room temperature up to 675°C with an ASC Scientific TD48 furnace. The natural remanent magnetization (NRM) was measured after each step with a 2G Enterprises 755 DC-SQUID cryogenic magnetometer located in a magnetically shielded room. The directions of the NRM were plotted on standard vector end-point demagnetization diagrams (Zijderveld, 1967) and the characteristic remanent magnetization (ChRM), where present, was isolated with standard principal component analysis of selected thermal demagnetization data. Backfield isothermal remanent magnetization (IRM) acquisition experiments were performed on 6 representative samples using an ASC Scientific IM-10-30 impulse magnetizer and an AGICO JR-6 spinner magnetometer. Thermal demagnetization of a three-component IRM (Lowrie, 1990) was performed on another set of 7 samples adopting 2.5 T, 0.4 T and 0.12 T orthogonal fields. Finally, the low-field magnetic susceptibility (κ) was measured with an AGICO KLY-3 Kappabridge. Two samples, representative respectively of the Wengen Fm. and San Cassiano Fm., have been selected for thermomagnetic experiments using an AGICO MFK1-FA Kappabridge with CS-3 furnace as well as hysteresis and first-order reverse curves (FORCs) using a PMC Micromag 3900 Vibrating Sample Magnetometer (VSM). The analyses were conducted at the Alpine Laboratory of

Paleomagnetism (ALP) of Peveragno (Italy) and the Laboratory of Paleomagnetism of ETH Zurich (Switzerland).

3.2 Magnetic properties

Values of remanent magnetization (J_{NRM}) and susceptibility (κ) at room temperature are relatively high throughout the section, with an average value of J_{NRM} = 64.5 x 10^{-3} A/m (Fig. 2C) and of κ = 61 x 10^{-4} SI (Fig. 2D). The highest values, with peaks of 300-370 x 10^{-3} A/m for J_{NRM} and 460-470 x 10^{-4} SI for κ, are observed in the lower-medium part of the section, where the volcaniclastic fraction is abundant (Fig. 2C, D). The backfield IRM acquisition curves (Fig. 4A; data in Supplementary Tab. S1) show the dominance of low coercivity phases (40 – 80 mT) with saturation reached between 100 and 300 mT, suggesting the presence of magnetite and/or maghemite. The presence of magnetite is evident also from the three-axis IRM experiments (Fig. 4B; data in Supplementary Tab. S1). The intermediate-coercivity 0.4 T curve shows a decay starting from 475-500°C and reaching a maximum unblocking temperature of ~600°C in most of the samples, coherent with the presence of a mixture of magnetite and hematite (Fig. 4B). The hard-coercivity 2.5 T curve, which carries a very small amount of the remanence, shows instead a maximum unblocking temperature of ca. 625-675°C, confirming the presence of hematite (Fig. 4B). The low-coercivity 0.12 T curve, which carries most of the remanence, shows a more complex behavior (Fig. 4B). Magnetization (J) rapidly decrease from room temperature up to 375-400°C, probably due to the presence of maghemite. Then, a more gradual reduction of J up to 500-575°C, indicating the presence of magnetite, is followed by a rapid decrease and complete demagnetization between 600°C and 625°C, suggesting a tail of secondary hematite, probably very fine-grained and superparamagnetic (Roberts et al., 2020).

The thermomagnetic curve of sample PG21 (Fig. 5) shows a dramatic decrease in susceptibility during the heating process between ca. 470°C and ca. 570°C followed by a slower decrease up to 650°C. This indicates the presence of magnetite/maghemite and hematite. The cooling curve is not

reversible and shows reduced susceptibility values (Fig 5). In the thermomagnetic experiment of sample PG80 (Fig. 5) susceptibility starts decreasing from ca. 550°C up to 650°C, suggesting the presence of a mixture of magnetite and hematite. The cooling curve is not reversible and shows magnetic enhancement (Fig. 5).

The hysteresis curves of samples PG21 and PG80 (Fig. 6A) indicate values of H_C (coercivity) of 8.4 mT (PG21) and 9.6 mT (PG80) J_R (magnetization of remanence) of 4.9 x 10^{-3} Am^2/kg (PG21) and ca. 6.6 x 10^{-4} Am^2/kg (PG80), J_S (magnetization of saturation after correction for paramagnetic contribution) of 3.9 x 10^{-2} Am^2/kg (PG21) and ca. 4.2 x 10^{-3} Am^2/kg (PG80). The coercivity of remanence (H_{CR}), obtained from backfield demagnetization experiments, is estimates between 25 and 30 mT for both samples. The Day-Dunlop plot (Day et al., 1977; Dunlop, 2002) in Fig. 6B shows that the ferromagnetic grains of PG21 and PG80 fall in the Pseudo Single Domain (PSD) area (Day et al., 1977; Dunlop, 2002) or the single domain (SD)+multi domain (MD) mixing area above ca. 70-80% of MD contribution (Dunlop, 2002).

The shape of the processed first-order reversal curves (FORCs) of PG21 and PG80 (Fig. 7) are compatible with the presence of low-coercivity PSD particles (Roberts et al., 2000), with a coercivity of ~60 mT. A discrete contribution of multi-domain (MD) particles is present in both samples.

In summary, the magnetic mineralogy of the Punta Grohmann stratigraphic sequence is represented by a mixture of magnetite and hematite, where magnetite seems to be the main carrier of remanence among the analyzed samples.

3.3 Magnetostratigraphy

Characteristic remanent magnetization (ChRM) component directions, scattered but generally oriented either north-and-down or south-and-up in both *in situ* and tilt-corrected coordinates, have been isolated in 56 out of a total of 93 samples from the Punta Grohmann section (Fig. 8) in a temperature range from a minimum of 150°C to a maximum of 675°C. The mean ChRM direction

in tilt-corrected coordinates, calculated by applying standard Fisher statistics on n = 56 ChRM directions, is Dec.: 6.4°E, Inc.: 40.5°, α_{95} = 9°, k = 5.5 (Tab. 2, Fig. 9). The high directional scattering of the ChRM component directions, frequently observed in medium- to coarse-grained sediments deposited in high- to variable-energy depositional systems and interpretable as due to grains mobility and interactions that tend to disturb the alignment of ferromagnetic particles imparted by the (weak) Earth's magnetic field, prevents accurate calculations of paleolatitude and paleopole position. However, we believe that the dual-polarity structure of the ChRM as revealed by alignments of thermal demagnetization steps provides sufficient information for polarity attribution and magnetostratigraphy.

Virtual Geomagnetic Poles (VGPs) have been calculated for each ChRM component direction and plotted relative to stratigraphic depth (Fig. 2E; ChRM and VGP data in Supplementary Tab. S2). Acknowledging from general paleogeography that during the Ladinian-Carnian the Dolomites were located in the northern hemisphere (e.g., Muttoni et al., 2013), the latitude of the sample VGP (positive for normal polarity, negative for reverse polarity) was used for interpreting the polarity stratigraphy. The VGP latitudes define 8 magnetozones, four of normal polarity and four of reverse polarity, named from base to top from GR1 to GR4 (Fig. 2E). The grey interval of uncertain polarity within GR1r (Fig. 2E) is due to the poor sample recovery and the low-quality record of the ChRM in this particular interval.

4. Correlations with key sections from the literature

4.1 Magnetostratigraphic correlation of Punta Grohmann with key Ladinian-Carnian sections

Ladinian magnetostratigraphy, in literature, is mainly represented by a series of key stratigraphic sections, such as: Prati di Stuores (northern Italy; Mietto et al., 2012), Mayerling (Austria; Gallet et al., 1998), Rio Nigra (northern Italy; Maron et al., 2019), Wayao (South China; Zhang et al., 2015), Gammstein 1 (Austria; Gallet et al., 1998), Mendlingbach West (Austria; Gallet et al., 1998), Aghia Triada (Greece; Muttoni et al., 1997), Frötschbach (northern Italy; Muttoni et al., 1997) and Seceda

(northern Italy; Muttoni et al., 2004) (Fig. 10). These sections have been used by Maron et al. (2019) to propose a new Geomagnetic Polarity Time Scale (GPTS) for the Triassic, where Seceda, Mayerling, Prati di Stuores (Carnian GSSP; Mietto et al., 2012) and Wayao have been used as reference sections for the Ladinian-Carnian portion of the GPTS. Following the magnetostratigraphic correlations proposed in Maron et al. (2019), the lower part of the Seceda section, where the Anisian/Ladinian boundary corresponds to the FAD of ammonoid *Eoprotrachiceras curionii*, is correlated with Frötschbach, Aghia Triada, and Mendlingbach West (Fig. 10). The magnetostratigraphy of Seceda is also coherent with Gammstein 1, where the SC4n to SC6n interval in Seceda and the GS3n to GS4n interval in Gammstein 1 can be both correlated to the lower part of Mayerling (MA1n to MA3n interval) (Fig. 10). The Mayerling section can also be correlated with Prati di Stuores, with the MA4r-MA5r interval corresponding to the S1r-S13r interval (Fig. 10). Magnetozones S3r and S4n of Prati di Stuores corresponds to the WA2r and WA3n of the astronomically-tuned (405 kyr and 100 kyr eccentricity cycles; Zhang et al., 2015) Wayao composite section (Fig. 10).

Starting from the correlation framework just described, the Punta Grohmann section can be correlated to the Prati di Stuores section (GSSP of the Carnian Stage; Mietto et al., 2012) through bio- and magnetostratigraphy. The boundary between the Regoledanus and Canadensis ammonoid Subzones marking the Ladinian/Carnian boundary is recognized at Prati di Stuores by the FAD of *Daxatina canadensis* (Broglio Loriga et al., 1999; Mietto et al., 2012), while at Punta Grohmann it is approximated by the FO of *Zestoceras lorigae* (Figs. 2, 10). Magnetozones GR3n, GR3r and GR4n at Punta Grohmann can be correlated to Prati di Stuores magnetozones S1n, S1r and S2n, respectively (Fig. 10). Following this correlation, the Ladinian/Carnian boundary, placed close to the base of magnetozone S2n at Prati di Stuores (Broglio Loriga et al., 1999; Mietto et al., 2012), can be projected to the base of GR4n at Punta Grohmann, broadly corresponding to the FO of *Z. lorigae* (Fig. 10).

The Punta Grohmann section can also be correlated through magnetostratigraphy with the Mayerling section in Austria (Gallet et al., 1998). Magnetozones GR2n, GR2r and GR3n at Punta Grohmann can be correlated to magnetozone MA4n straddling sub-magnetozone MA4n.1r at Mayerling (Fig. 10). Then, magnetozone GR3r can be correlated to MA4r. There seems to be no thick reverse magnetozone at Mayerling that could be readily correlated to GR1r at Punta Grohmann. However, sedimentation rates are likely to be much higher in the lower part of the Punta Grohmann section (0-320 m), characterized by abundant siliciclastic turbidites (Wengen Fm.), than at Mayerling, where pelagic carbonate deposition dominates (Gallet et al., 1994, 1998). Hence, we propose to correlate magnetozone GR1r to MA3r (Fig. 10).

The Rio Nigra section hosting the U-Pb age of 237.77 ± 0.05 Ma was correlated by Maron et al. (2019) to Mayerling by considering magnetozone RN1r at Rio Nigra equivalent to MA3r at Mayerling (see figure 12 in Maron et al., 2019). Here we revise this correlation (Fig. 10). Considering that the Wengen-like strata comprising the Rio Nigra section (Frommer Mb. of the Fernazza Fm.) could have high accumulation rates similar to the Wengen Fm. of the Punta Grohmann section, then the comparatively thin RN1r magnetozone at Rio Nigra seems unlikely correlative to MA3r at Mayerling or to G1r at Punta Grohmann. Alternatively, the RN1n-RN2n polarity interval at Rio Nigra could entirely be included within magnetozone MA3n at Mayerling (Fig. 10).

This new interpretation is in agreement with the Neumayri/Regoledanus ammonoid subzones boundary that has been registered in Rio Nigra (Maron et al., 2019) and that has been inferred for Mayerling by Maron et al. (2019) through the comparison of the conodont and ammonoid biostratigraphic scales from the Reifling Basin of Austria, to which Mayerling belongs, and the Dolomites (Krystyn, 1983; Mietto and Manfrin, 1995a; Gallet et al., 1998; Hochuli et al., 2015) (Fig. 10).

Finally, according to recent lithostratigraphic analyses and regional correlations, the Rio Nigra section could altogether fall within the unconformity that at Punta Grohmann marks the boundary

between the volcanites of the Fernazza Fm. and the Marmolada Cgm. (Storck et al., 2019; Gianolla et al., 2021) (Fig. 1B), pointing to an older age of the Rio Nigra magnetostratigraphy with respect to Punta Grohmann (Fig. 10).

4.2 Age of the Ladinian/Carnian boundary

The U-Pb ages obtained from the ash-bed at ca. 220 m in the Punta Grohmann section (237.58 ± 0.04 Ma and 237.68 ± 0.05 Ma; Storck et al., 2019) are used in association with the radiometric ages from Seceda (Wotzlaw et al., 2018) to estimate the age of the Ladinian/Carnian boundary (Tab. 3). The pelagic marine section of Mayerling, characterized by a more continuous magnetostratigraphy across the Ladinian/Carnian boundary interval (marked by the FAD of conodont *Paragondolella polygnathiformis*; Gallet et al., 1998), can be used as reference section for this interval onto which to project the aforementioned U-Pb ages by means of magnetostratigraphic correlations. Following the correlation in Figure 10, the radiometric age of 239.04 ± 0.10 Ma at the base of SC5n at Seceda (Wotzlaw et al., 2018) is projected at the base of MA2n at Mayerling (Fig. 10; Tab. 3), coherently with the Seceda-Mayerling correlation in Maron et al. (2019).

The U-Pb age of Rio Nigra (237.77 ± 0.05 Ma; Mietto et al., 2012) cannot be precisely projected onto Mayerling albeit according to our revised correlation, it should fall somewhere within MA3n.

The radiometric ages of Punta Grohmann can be projected within Mayerling magnetozone MA3r (Fig. 10; Tab. 3). Mayerling and Prati di Stuores have been correlated after Maron et al. (2019), and accordingly, the Ladinian/Carnian boundary, as defined at Prati di Stuores (FAD of ammonoid *Daxatina canadensis*), has been projected within MA5n at Mayerling. Assuming a substantially uniform sediment accumulation rate for Mayerling, the age of the Carnian base (FAD of *D. canadensis*) is here estimated at 236.5 Ma (Fig. 11; Supplementary Tab. S3). An error of ± 0.1 Ma have been estimated by the sum in quadrature of the errors of the U-Pb ages used as tie-points (Tab. 3; Supplementary Tab. S3). The reconstructed magnetochronology of the Ladinian-Carnian interval implies very high long-term sedimentation rates in the lower part of the Punta Grohmann section up

to ~321 m (~1306 m/Myr; Fig. 11), followed by progressively lower rates of ~211 m/Myr and ~156 m/Myr up to ~470 m, and a final increase up to 274 m/Myr in the uppermost part of the section (Fig. 11). These are long-term rates averaged over extended stratigraphic intervals characterized by different facies, so it is likely for example that the lowermost part of the section (0 – 170 meters) made by turbidites and carbonate megabreccias (representing the FSST and LST) is characterized by even higher sedimentation rates.

High rates of sediment accumulation (more than 1000 m/Myr) are not uncommon in turbiditic basins, especially if confined (e.g., Marini et al., 2020).

In this respect, a possible explanation of the high accumulation rates observed in the lower part of the section is the filling of a confined (ponded) basin, whereas the generally lower rates observed upsection could be due to the consequent spillover of the turbiditic sediments once the basin is completely filled. The slight increase of the sedimentation rates in the uppermost part of the section (above ~470 m; Fig. 11), characterized by the input of coarse-grained sediments (calcarenites and sandy marlstones) and the presence of carbonate breccias (Fig. 2A), is coherent with the progradation of the Cassian carbonate platform of the Sassolungo/Langkofel massif over the basinal deposits of the San Cassiano Fm. (e.g., Mietto et al., 2012; Storck et al., 2019; Gianolla et al., 2021).

5. Conclusions

The magnetostratigraphy of the Punta Grohmann section, provided with U-Pb ages of 237.58 ± 0.04 Ma and 237.68 ± 0.05 Ma (Storck et al., 2019), represents an opportunity to calibrate the Triassic Geomagnetic Polarity Time Scale (GPTS) around the Ladinian/Carnian boundary, and update the age of the base of the Carnian. As in the compilation of the Triassic GPTS of Maron et al. (2019), we used the Mayerling section (Northern Calcareous Alps, Austria) as a reference section to calibrate the age of the base of the Carnian, because this pelagic section has a continuous stratigraphy and a relatively constant sediment accumulation rate. Projecting the U-Pb ages of Punta

Grohmann (Storck et al., 2019) and Seceda (Wotzlaw et al., 2018) into the Mayerling reference magnetostratigraphy, we obtained an age for the Ladinian/Carnian boundary of ~236.5 (± 0.1) Ma, which is ~500-300 kyr younger than previously estimated (e.g., Mietto et al., 2012; Maron et al., 2019). Beyond the chronological implications of the magnetostratigraphy, the sediment accumulation rates estimated for the Punta Grohmann section reveal the complex post-volcanic topography of this area during the uppermost Ladinian and its influence on the sedimentation of the Wengen Formation.

Acknowledgements

We wish to thank Ann M. Hirt for allowing MM to perform VSM measurements at the paleomagnetics laboratory of ETH Zurich, Manuel Rigo for valuable suggestions that improved this manuscript, Stefano Manfrin for helping with the classification of ammonoids, Guido Roghi for the suggestion on palynostratigraphy, Marica Ghezzi for her valuable help during the fieldwork, and photographer Matteo Visintainer for the high-definition pictures of the Punta Grohmann section. Thanks to Editor, Reviewer #1 (Prof. Peter Brack) and anonymous Reviewer #2 for their valuable comments that helps us improve this paper. This study has benefited from financial support of IAS (International Association of Sedimentologists) Post-doctoral Research Grant 2016 to M. Maron.

References

Balini M., Germani D., Nicora A., Rizzi E., 2000. Ladinian/Carnian ammonoids and conodonts from the classic Schilpario-Pizzo Camino area (Lombardy): revaluation of the biostratigraphic support to chronostratigraphy and paleogeography. Rivista Italiana di Paleontologia e Stratigrafia, 106, 19-58.

Bosellini, A., Castellarin, A., Doglioni, C., Guy, F., Perri, M.C., Rossi, P.M., Simboli, G., Sommavilla, E., 1982. Geologia della Conca di Arabba e dei rilievi circostanti, in:

Castellarin, A., Vai, G.B. (Eds.), Guida alla Geologia del Sudalpino Centro-Orientale. Guide Geol. Reg. S.G.I., pp. 243–254.

Brandner, R., Keim, L., 2011. A 4-day geological field trip in the Western Dolomites. Geo.Alp. 8, 76–118.

Broglio Loriga C., Cirilli S., De Zanche V., di Bari D., Gianolla P., Laghi M.F., Lowrie W., Manfrin S., Mastandrea A., Mietto P., Muttoni C., Neri C., Posenato C., Rechichi M.C., Rettori R., Roghi G., 1998. The Prati di Stuores/Stuores Wiesen section (Dolomites, Italy): as GSSP candidate for the Ladinian-Carnian boundary. Pralongià Meeting 2-3 July 1998, 62 pp.

Broglio Loriga, C., Cirilli, S., De Zanche, V., Di Bari, D., Gianolla, P., Laghi, G.F., Lowrie, W., Manfrin, S., Mastandrea, A., Mietto, P., Muttoni, G., Neri, C., Posenato, R., Rechichi, M., Rettori, R., Roghi, G., 1999. The Prati di Stuores/Stuores Wiesen section (Dolomites, Italy): a candidate Global Stratotype Section and Point for the base of the Carnian Stage. Rivista Italiana di Paleontologia e Stratigrafia 105, 37-78.

Buryi, G.I., 1989. Triassic conodonts and stratigraphy of Sikhote-Alin. Vladivostok, FEB Academy of Sciences of the USSR, 136 pp.

Castellarin, A., Selli, L., Picotti, V., Cantelli, L., 1998. Tettonismo e diapirismo Medio-Triassico delle Dolomiti. Memorie Società Geologica Italiana 53, 145-169.

Day, R., Fuller, M., Schmidt, V.A., 1977. Hysteresis properties of titanomagnetites: grain-size and compositional dependence. Physics of Earth and Planetary Interiors 13, 260-267. https://doi.org/10.1016/0031-9201(77)90108-X

De Zanche, V., Gianolla, P., 1995. Litostratigrafia al limite Ladinico-Carnico nel Sudalpino orientale. Annali dell'Università di Ferrara, Scienze della Terra 5, 41-48.

Diebel, K., 1956. Conodonten in der Oberkreide von Kamerun. Geologie 5, 424-450.

Dunlop, D.J., 2002. Theory and application of the Day plot (M_{rs}/M_s versus H_{cr}/H_c) 1. Theoretical curves and tests using titanomagnetite data. Journal of Geophysical Research 107, EPM4-1 EPM4-22. https://doi.org/10.1029/2001JB000487

Egli, R., 2013. VARIFORC: An optimized protocol for calculating non-regular first-order reversal curve (FORC) diagrams. Global and Planetary Change 110, 302-320. https://doi.org/10.1016/j.gloplacha.2013.08.003

Gallet, Y., Besse, J., Krystyn, L., Théveniaut, H., Marcoux, J., 1994. Magnetostratigraphy of the Mayerling section (Austria) and Erenkolu Mezarlik (Turkey) section: Improvement of the Carnian (late Triassic) magnetic polarity time scale. Earth and Planetary Science Letters 125, 173-191. https://doi.org/10.1016/0012-821X(94)90214-3

Gallet, Y., Krystyn, L., Besse, J., 1998. Upper Anisian to Lower Carnian magnetostratigraphy from the Northern Calcareous Alps (Austria). Journal of Geophysical Research 103, 605-621. https://doi.org/10.1029/97JB02155

Gianolla, P., De Zanche, V., Mietto, P., 1998. Triassic sequence stratigraphy in the southern Alps (northern Italy): definition of sequences and basin evolution, in: De Gracianky, P.C., Jacquin, T., Vail, P.R. (Eds.), Mesozoic and Cenozoic sequence stratigraphy of European basins. S.E.P.M. Special Publications 60, pp. 719-747.

Gianolla, P., Caggiati, M., Riva, A., 2021. The interplay of carbonate systems and volcanics: Cues from the 3D model of the Middle Triassic Sciliar/Schlern platform (Dolomites, Southern Alps). Marine and Petroleum Geology 124, 104794. https://doi.org/10.1016/j.marpetgeo.2020.104794

Harrison, R.J., Feinberg, J.M., 2008. FORCinel: An improved algorithm for calculating first-order reversal curve distribution using locally weighted regression smoothing. Geochemistry, Geophysics, Geosystems 9, Q05016. https://doi.org/10.1029/2008GC001987

Hauer, F., Von., 1860. Nachtraege zur Kenntniss der Cephalopoden-Fauna der Hallstaetter Schichten. Sitzungberichte der Akademie der Wissenschaften in Wien (I) 41, 113-150.

Hochuli, P.A., Roghi, G., Brack, P., 2015. Palynological zonation and particulate organic matter of the Middle Triassic of the Southern Alps (Seceda and Val Gola-Margon sections, Northern Italy). Review of Palaeobotany and Palynology 218, 28-47. https://doi.org/10.1016/j.revpalbo.2014.07.006

Huckriede, R. 1958. Die Conodonten der Mediterranen Trias und ihr stratigraphischer Wert. Palaeontologische Zeitschrift 32, 141-151.

Klaus, W., 1960. Sporen der karnischen Stufe der ostalpinen Trias. Jahrbuch der Geologischen Bundesanstalt 5, 107-184.

Kovacs, S., 1983. On the evolution of *excelsa*-stock in the Upper Ladinian-Carnian (Conodonta, genus *Gondolella*, Triassic). Schriftenreihe der Erdwissenschaftlichen Kommissionen 5, 107–120.

Kozur, H., Mock, R., 1972. Neue Conodonten aus der Trias der Slowakei und ihre stratigraphische Bedeutung. Geologische-Paläontologische Mitteilungen Innsbruck 2, 1-20.

Krystyn, L., 1983. Das Epidaurus-Profil (Griechenland) – ein Beitrag zur Conodonten-Standardzonierung des tethyalen Ladin un Unterkarn. In: Zapfe, H. (Ed.), Neue Beiträge zur Biostratigraphie der Tethys-Trias. Schriftenreihe der Erdwissenschaftlichen Kommissionen, Österreichisches Akademie der Wissenschaften 5, 231-258.

Leschik, G., 1956. Die Keuperflora von Neuewelt bei Basel. II. Die iso-und mikrosporen. Schweizerische Paläontologische Abhandlungen 72, 1-70.

Lowrie, W., 1990. Identification of ferromagnetic minerals in a rock by coercivity and unblocking temperature properties. Geophyisical Research Letters 17, 159-162. https://doi.org/10.1029/GL017i002p00159

Maron, M., Muttoni, G., Rigo, M., Gianolla, P., Kent, D.V., 2019. New magnetobiostratigraphic results from the Ladinian of the Dolomites and implications for the Triassic geomagnetic polarity timescale. Palaeogeography, Palaeoclimatology, Palaeoecology 517, 52-73. https://doi.org/10.1016/j.palaeo.2018.11.024

Marini, M., Maron, M., Petrizzo, M.R., Felletti, F., Muttoni, G., 2020. Magnetochronology applied to assess tempo of turbidite deposition: A case study of ponded sheet-like turbidites from the lower Miocene of the northern Apennines (Italy). Sedimentary Geology 403, 105654. https://doi.org/10.1016/j.sedgeo.2020.105654

McLearn, F.H., 1947. Upper Triassic faunas of Pardonet Hill, Peace River Foothills, British Columbia. Geological Survey of Canada Paper 47(14), 1-16.

Mietto, P., Manfrin, S., 1995a. A high resolution Middle Triassic ammonoid standard scale in the Tethys Realm. A preliminary report. Bulletin de la Société Géologique de France 166, 539-563.

Mietto, P., Manfrin, S., 1995b. La successione delle faune ad ammonoidi al limite Ladinico-Carnico (Sudalpino, Italia). Annali dell'Università di Ferrara, Scienze della Terra 5, 13-35.

Mietto, P., Manfrin, S., Preto, N., Gianolla, P., 2008. Selected ammonoid fauna from Prati di Stuores/Stuores Wiesen and related sections across the Ladinian-Carnian boundary (southern Alps, Italy). Rivista Italiana di Paleontologia e Stratigrafia 114, 377-429. https://doi.org/10.13130/2039-4942/5909

Mietto, P., Manfrin, S., Preto, N., Rigo, M., Roghi, G., Furin, S., Gianolla, P., Posenato, R., Muttoni, G., Nicora, A., Buratti, N., Cirilli, S., Spötl, C., Ramezani, J., Bowring, S.A., 2012. The Global Boundary Stratotype Section and Point (GSSP) of the Carnian Stage (Late Triassic) at Prati di Stuores/Stuores Wiesen section (southern Alps, NE Italy). Episodes 35, 414-430.

Mojsisovics, E.M. von, 1882. Die Cephalopoden der mediterranen Triasprovinz. Abhandlungen der Kaiserlich-Königlichen Geologischen Reichsanstalt 10, 1-332.

Mojsisovics E.M. von, 1893. Die Cephalopoden der Hallstätter Kalke. Abhandlungen der Kaiserlich-Königlichen Geologischen Reichsanstalt 6, 1–835.

Münster, G., 1834. Das Kalkmergellager von St. Cassian und die darin befindlichen Ceratiten. Leonhard u Bronn's Jahrbuch 1-15.

Muttoni, G., Kent, D.V., Brack, P., Nicora, A., Balini, M., 1997. Middle Triassic magnetostratigraphy and biostratigraphy from the Dolomites and Greece. Earth and Planetary Science Letters 146, 107-120. https://doi.org/10.1016/S0012-821X(96)00216-6

Muttoni, G., Nicora, A., Brack, P., Kent, D.V., 2004. Integrated Anisian–Ladinian boundary chronology. Palaeogeography, Palaeoclimatology, Palaeoecology 208, 85-102. https://doi.org/10.1016/j.palaeo.2004.02.030

Muttoni, G., Dallanave, E., Channell, J.E.T., 2013. The drift history of Adria and Africa from 280 Ma to Present, Jurassic true polar wander, and zonal climate control on Tethyan sedimentary facies. Palaeogeography, Palaeoclimatology, Palaeoecology 386, 415-435. https://doi.org/10.1016/j.palaeo.2013.06.011

Ogilvie-Gordon, M., 1927. Das Grödener-, Fassa- und Enneberggebiet in den Südtiroler Dolomiten. III Teil. Paläontologie. Abh. Geol. Reichsanst. 24/2, 1-89.

Roberts, A.P., Pike, C.R., Verosub, K.L., 2000. First-order reversal curve diagrams: a new tool for characterizing the magnetic properties of natural samples. Journal of Geophysical Research 105, 28461-28475. https://doi.org/10.1029/2000JB900326

Roberts, A.P., Zhao, X., Heslop, D., Abrajevitch, A., Chen, Y.-H., Hu, P., Jiang, Z., Liu, Q., Pillans, B.J., 2020. Hematite (α-Fe_2O_3) quantification in sedimentary magnetism: limitations of existing proxies and ways forward. Geoscience Letters 7, 8. https://doi.org/10.1186/s40562-020-00157-5

Russo, F., Neri, C., Mastandrea, A., Baracca, A., 1997. The mud mound nature of the Cassian Platform Margins of the Dolomites. A case history: the Cipit boulders from Punta Grohmann (Sasso Piatto Massif, northern Italy). Facies 36, 25-36. https://doi.org/10.1007/BF02536875

Scudeler Baccelle, L., 1974. La serie ladino-carnica alla base della Punta Grohmann (Gruppo del Sasso Lungo, Dolomiti occidentali): strutture sedimentarie e petrologia della facies carbonatica. Memorie di Geopaleontologia Università di Ferrara 3/2, 19-35.

Scheuring, B.W., 1970. Palynologische und palynostratigraphische Untersuchungen des Keupers im Bölchentunnel (Solothurner Jura). Schweizerische Paläontologische Abhandlungen 88, 2-119.

Schuurman, W.M., 1976. Aspects of Late Triassic palynology. 1. On the morphology, taxonomy and stratigraphical/geographical distribution of the form genus Ovalipollis. Review of Palaeobotany and Palynology 21 (4), 241–266.

Stefani, M., Furin, S., Gianolla, P., 2010. The changing climate framework and depositional dynamics of Triassic carbonate platforms from the Dolomites. Palaeogeography, Palaeoclimatology, Palaeoecology 290, 43-57. https://doi.org/10.1016/j.palaeo.2010.02.018

Storck, J.-C., Brack, P., Wotzlaw, J.-F., Ulmer, P., 2019. Timing and evolution of Middle Triassic magmatism in the Southern Alps (northern Italy). Journal of the Geological Society of London 176, 253-268. https://doi.org/10.1144/jgs2018-123

Tozer, E.T., 1972. Observations on the shell structure of Triassic ammonoids. Palaeontology 15 (4), 637-654.

Tozer, E.T., 1994. Canadian Triassic Ammonoid Faunas: Geological Survey of Canada, Bulletin 467, pp. 1-663.

Van der Boogaard, M., 1966. Post-Carboniferous conodonts from south-eastern Spain. Proceedings of the Koninklijke, Nederlandse Akademie Van Wetenschappen, Series B 69, 1-19

Van der Eem, J., 1983. Aspects of Middle and Late Triassic Palynology. Palynological Investigations in the Ladinian and Lower Karnian of the Western Dolomites, Italy. Review of Palaeobotany and Palynology 39, 189-300. https://doi.org/10.1016/0034-6667(83)90016-7

Whiteaves, J.F., 1889. On some fossils from the Triassic rocks of British Columbia. Geological Survey of Canada, Contributions to Canadian Palaeontology 1, 127-149.

Wotzlaw, J.-F., Brack, P., Storck, J.-C., 2018. High-resolution stratigraphy and zircon U–Pb geochronology of the Middle Triassic Buchenstein Formation (Dolomites, northern Italy):

precession-forcing of hemipelagic carbonate sedimentation and calibration of the Anisian–Ladinian boundary interval. Journal of the Geological Society of London 175, 71-85. https://doi.org/10.1144/jgs2017-052

Zhang, Y., Li, M., Ogg, J.G., Montgomery, P., Huang, C., Chen, Z.-Q., Shi, Z., Enos, P., Lehrmann, D.J., 2015. Cycle-calibrated magnetostratigraphy of middle Carnian from South China: Implications for Late Triassic time scale and termination of the Yangtze Platform. Palaeogeography, Palaeoclimatology, Palaeoecology 436, 135-166. https://doi.org/10.1016/j.palaeo.2015.05.033

Zijderveld, J.D.A., 1967. A.C. demagnetization of rocks: analysis of results, in: Collinson, D.W., Creer, K.M., Runcorn, S.K. (Eds.), Methods in Paleomagnetism. Elsevier, Amsterdam, pp. 254–286.

Figure Captions

Figure 1: A) Location of the Punta Grohmann section in the Dolomites of northern Italy; B) Bio-chrono-stratigraphic chart and stratigraphic relationship of Ladinian-Carnian Formations in the Western Dolomites (modified after Gianolla et al., 2021).

Figure 2: Magnetostratigraphy, rock-magnetic properties and biostratigraphy of the Punta Grohmann section: A) lithostratigraphy and sequence stratigraphy (Mietto et al., 2012; Gianolla et al., 2021; FSST is Falling Stage System Tract, LST is Lowstand System Tract, TST is Transgressive System Tract, HTS is Hightstand System Tract); samples for magnetostratigraphy are represented by red ticks; B) ammonoid (this study) and palynomorph (Van der Eem, 1983) biostratigraphy; C) NRM magnetization (J_{NRM}); D) magnetic susceptibility (κ); E) VGP latitudes, used to define a sequence of 8 magnetozones from GR1n to GR4r. The Ladinian/Carnian boundary is here approximated by the First Occurrence of ammonoid *Zestoceras lorigae*. The HST of Car-1 is generally attributed to the basal Carnian (Gianolla et al., 1998).

Figure 3: View of the Punta Grohmann outcrop from Col Rodella with indication of the sampling path followed to collect paleomagnetic samples as well as the position of the ash-bed providing the U-Pb ages of Storck et al. (2019) (A). In panel (B) a blow-up of the upper part of the section showing the position of relevant ammonoid-bearing levels GRH3, GRH90, and GRO10 located respectively at ~480 m, ~510 m, and ~530 m from the section base. Representative ammonoids coming from these levels are: *Frankites apertus* (GRH-3.1; panel C), *Carnites* sp. (GRO-10.5; panel D), *Trachyceras* sp. vel *Daxatina* sp. (GRO-10.7; panel E), and *Asklepioceras* sp. (GRH-90.1; panel F).

Figure 4: Isothermal Remanent Magnetization (IRM) experiments. Backfield IRM acquisition curves (A) indicate remanence coercivities (H_{cr}) of 40–80 mT and saturation remanences attained at 100-300 mT consistent with magnetite. Three-axis IRM thermal demagnetization curves (B) show a dominant soft coercivity (0.12 T) mineral phase interpreted as magnetite coexisting with (superparamagnetic?) hematite and a high-coercivity (2.5 T) phase interpreted as hematite. Detail of the high temperature interval between 540°C and 680°C is shown for each sample.

Figure 5: Heating and cooling curves of magnetic susceptibility of samples PG21 (Wengen Fm.) and PG80 (San Cassiano Fm.). Heating curve of PG21 shows a dramatic drop in susceptibility after 470°C, indicative of magnetite, and a maximum Curie temperature T_C = 650°C, indicative of hematite. Similar data are obtained from the heating of sample PG80, with a rapid drop of susceptibility after 550°C (magnetite) and a maximum T_C of 650°C (hematite).

Figure 6: Hysteresis curves (A) and derived parameters Jr/Js vs. Hcr/Hc (B) of samples PG21 (Wengen Fm.) and PG80 (San Cassiano Fm.). The hysteresis parameters are consistent with PSD magnetite or SD+MD magnetite mixtures (Day et al., 1977; Dunlop, 2002).

Figure 7: First-order reversal curve (FORC) diagrams of PG21 (Wengen Fm.; panel A) and PG80 (San Cassiano Fm.; panel B). In both diagrams, the shape of the central ridge is typical of

PSD or a mixture of SD+MD magnetite. The contours of samples PG80 are more dispersed, probably because of more abundant MD grains in the mixture. FORCs have been processed using VARIFORC (Egli, 2013) integrated in FORCinel (Harrison and Feinberg, 2008).

Figure 8: Vector end-point thermal demagnetization diagrams of representative samples from Punta Grohmann. Open/closed symbols represent projections onto the horizontal/vertical axis. Thermal demagnetizations in °C.

Figure 9: Equal area projection of the ChRM component directions of the Punta Grohmann samples. The ChRM component directions are scattered in both *in situ* and tilt-corrected coordinates, although generally distributed either to the north-and-down or to the south-and-up. These directions have been used to calculate VGP latitudes in Figure 2E and derive the magnetostratigraphy of the Punta Grohmann section.

Figure 10: Correlation between Punta Grohmann and key Ladinian/Early Carnian magnetostratigraphic sections from the literature used by Maron et al. (2019) to define the Ladinian–Carnian portion of the Triassic Geomagnetic Polarity Time Scale (GPTS): Prati di Stuores (northern Italy; Mietto et al., 2012), Mayerling (Austria; Gallet et al., 1998), Rio Nigra (northern Italy; Maron et al., 2019), Wayao (South China; Zhang et al., 2015), Gammstein 1 (Austria; Gallet et al., 1998), Mendlingbach West (Austria; Gallet et al., 1998), Aghia Triada (Greece; Muttoni et al., 1997), Frötschbach (northern Italy; Muttoni et al., 1997) and Seceda (northern Italy; Muttoni et al., 2004). Radiometric ages from Seceda are after Wotzlaw et al. (2018), from Rio Nigra after Mietto et al. (2012), and from Punta Grohmann after Storck et al. (2019). We used data from Punta Grohmann accompanied by a revised correlation between Rio Nigra and Mayerling to update the Ladinian–Carnian portion of the Triassic Geomagnetic Polarity Time Scale of Maron et al. (2019). The age of the Ladinian/Carnian boundary is here recalculated at ca. 236.5 Ma from a previous estimate of 236.8 Ma (Maron et al., 2019). See text for discussion.

Figure 11: Magnetostratigraphy (in meters) of the Punta Grohmann section plotted against the Ladinian–Carnian Geomagnetic Polarity Time Scale of this study, implying very high long-term (average) sedimentation rates in the lower part of the section followed upsection by lower values and a final increase in the uppermost part of the section. These accumulation rates are compatible with the infilling of a small, ponded basin (e.g., Marini et al., 2020). The error interval around the average sedimentation rate values is indicated by the grey area (see Tab. S3 for calculation).

Table Captions

Table 1: Ammonoid distribution in the Punta Grohmann section.

Table 2: *In situ* and tilt-corrected ChRM component mean direction and associated Fisher statistics of Punta Grohmann samples.

Table 3: Radiometric ages (with errors) used as tie-points to calculate the age of the Carnian base.

Supplementary material

Table S1: Thermal demagnetization of three-axis IRM and backfield acquisition of IRM of Punta Grohmann samples.

Table S2: ChRM component directions and VGP latitudes of Punta Grohmann samples.

Table S3: Age model of the Punta Grohmann section and relative error calculation.

TABLE 1. Ammonoid distribution in the Punta Grohmann section

BEDS	*Maclearnoceras* sp.	cf. *Joannites* sp.	*Lecanites glaucus* (Münster)	*Lobites ellipticus* (Hauer)	*Frankites apertus* (Mojsisovics)	*Frankites* cf. *apertus* (Mojsisovics)	*Frankites* sp.	*Orestites* sp.	*Celtites* sp.	*Asklepioceras* sp.	*Celtites epolensis* (Mojsisovics)	cf. *Frankites* sp.	cf. *Protrachyceras* sp.	*Celtites* sp. A	*Carnites* sp.	*Trachyceras* sp. vel *Daxatina* sp.	*Zestoceras lorigae* (Mietto & Manfin)	TOTAL	BIOZONES	STAGES
GRO10					2		1							3	1	2	4	13	Canadensis Sbz.	JULIAN
GRH90										1								1	Regoledanus Sbz.	LONGOBARDIAN
GRH80											4	1	1					6		
GRH3					1													1		
GRH8									1	1								2		
GRH7							1	1										2		
GRH2c						2												2		
GRH2b			1															1		
GRH2a			2		1													3		
GRH100			1	1														2		
GRH9b			1															1		
GRH9a		1																1		
GRH1	2																	2		
TOTAL	2	1	5	1	4	2	2	1	1	2	4	1	1	3	1	2	4	37		
BEDS	*Maclearnoceras* sp.	cf. *Joannites* sp.	*Lecanites glaucus* (Münster)	*Lobites ellipticus* (Hauer)	*Frankites apertus* (Mojsisovics)	*Frankites* cf. *apertus* (Mojsisovics)	*Frankites* sp.	*Orestites* sp.	*Celtites* sp.	*Asklepioceras* sp.	*Celtites epolensis* (Mojsisovics)	cf. *Frankites* sp.	cf. *Protrachyceras* sp.	*Celtites* sp. A	*Carnites* sp.	*Trachyceras* sp. vel *Daxatina* sp.	*Zestoceras lorigae* (Mietto & Manfin)	TOTAL	BIOZONES	STAGES

TABLE 1. Paleomagnetic mean directions of the Punta Grohmann section

MEAN DIRECTIONS									
		In Situ				Tilt-Corrected			
Site	N	k	α_{95}	Dec.	Inc.	k	α_{95}	Dec.	Inc.
Punta Grohmann	56	5.4	9.1°	17.3°E	61.6°	5.5	9.0°	6.4°E	40.5°

Note: N: number of samples Dec.: mean Declination Inc.: mean Inclination

k: Fisher precision parameter α_{95}: radius of the 95% confidence cone

TABLE 3. Tie-points for Carnian Age calculation

Age (Ma)	Section	Reference	Original Magnetozone	Relative Mayerling Magnetozone
239.04±0.10	Seceda	Wotzlaw et al., 2017	SC5n	MA2n
237.58±0.04	Punta Grohmann	Storck et al., 2019	GR1r	MA3r
237.68±0.05	Punta Grohmann	Storck et al., 2019	GR1r	MA3r

Declaration of interests

☒The authors declare that they have no known competing financial interests or personal relationships that could have appeared to influence the work reported in this paper.

☐The authors declare the following financial interests/personal relationships which may be considered as potential competing interests:

Highlights

- New magnetostratigraphic data of a U-Pb constrained Ladinian section improves Triassic chronology.
- The Punta Grohmann time-calibrated magnetostratigraphic data has been used to update the Geomagnetic Polarity Timescale of the late Ladinian.
- Updated Geomagnetic Polarity Timescale led to a revised age of the Ladinian/Carnian boundary (~236.5 Ma).

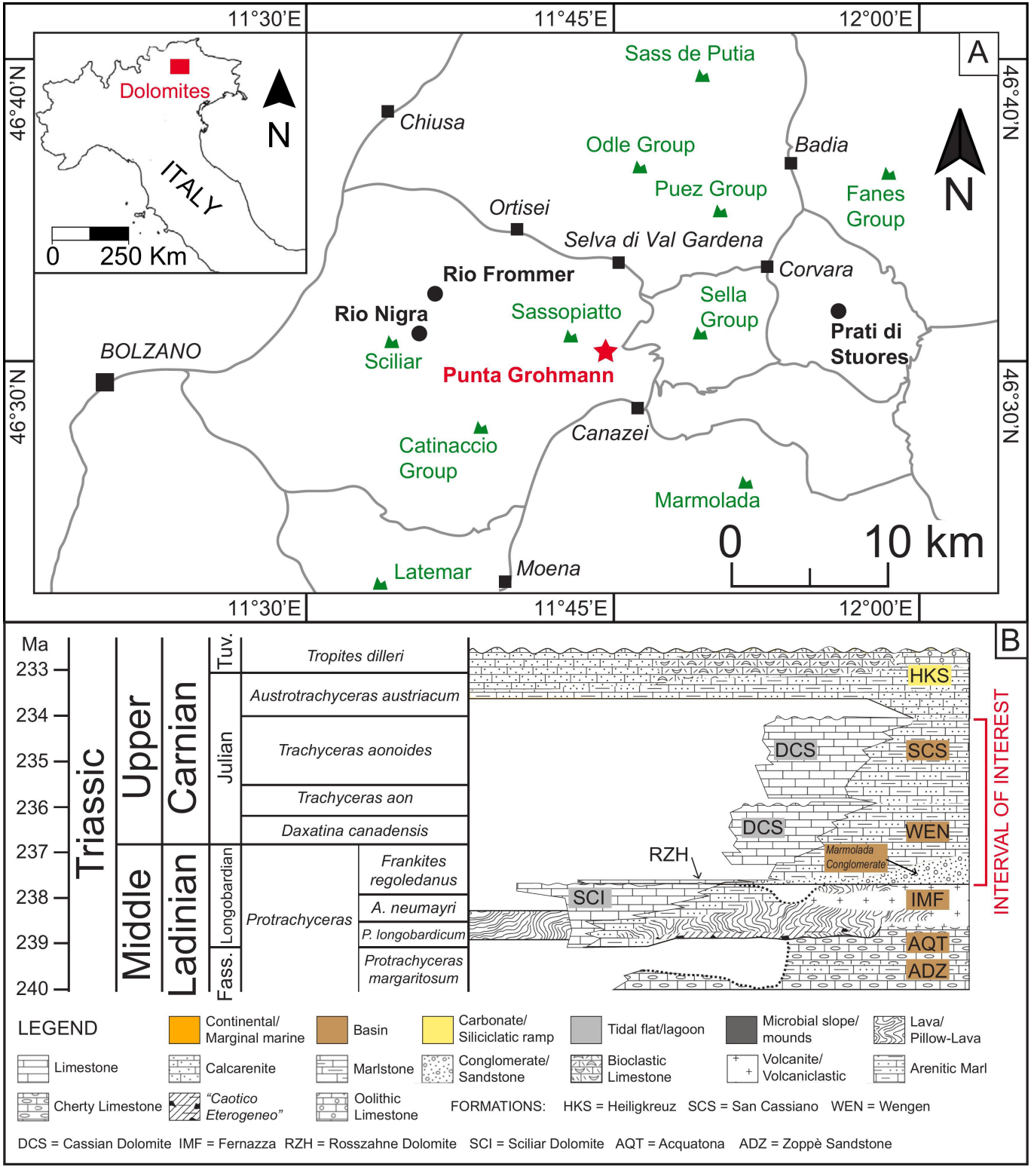
11°30'E
11°45'E
12°00'E
46°40'N
46°30'N
A
Dolomites
ITALY
N
0 250 Km
Sass de Putia
Chiusa
Odle Group
Badia
Puez Group
Fanes Group
Ortisei
Selva di Val Gardena
Corvara
Rio Frommer
Rio Nigra
Sassopiatto
Sella Group
Prati di Stuores
BOLZANO
Sciliar
Punta Grohmann
Canazei
Catinaccio Group
Marmolada
0 10 km
Latemar
Moena
B
Ma
233
234
235
236
237
238
239
240
Triassic
Upper
Middle
Carnian
Ladinian
Tuv.
Julian
Longobardian
Fass.
Tropites dilleri
Austrotrachyceras austriacum
Trachyceras aonoides
Trachyceras aon
Daxatina canadensis
Protrachyceras
Frankites regoledanus
A. neumayri
P. longobardicum
Protrachyceras margaritosum
HKS
DCS
SCS
DCS
WEN
Marmolada Conglomerate
RZH
SCI
IMF
AQT
ADZ
INTERVAL OF INTEREST
LEGEND
Continental/ Marginal marine
Basin
Carbonate/ Siliciclatic ramp
Tidal flat/lagoon
Microbial slope/ mounds
Lava/ Pillow-Lava
Limestone
Calcarenite
Marlstone
Conglomerate/ Sandstone
Bioclastic Limestone
Volcanite/ Volcaniclastic
Arenitic Marl
Cherty Limestone
"Caotico Eterogeneo"
Oolithic Limestone
FORMATIONS: HKS = Heiligkreuz SCS = San Cassiano WEN = Wengen
DCS = Cassian Dolomite IMF = Fernazza RZH = Rosszahne Dolomite SCI = Sciliar Dolomite AQT = Acquatona ADZ = Zoppè Sandstone

Figure 1

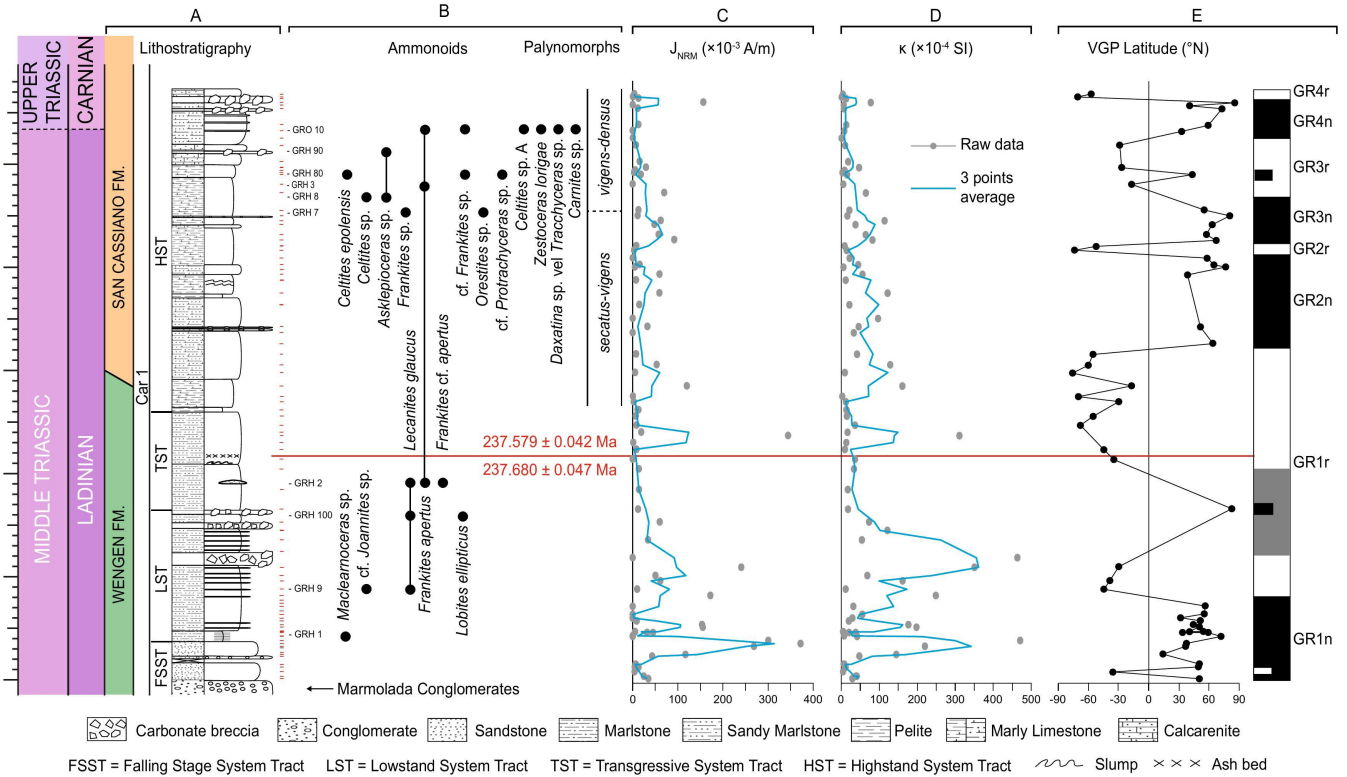
A
B
C
D
E
Lithostratigraphy
Ammonoids
Palynomorphs
J_{NRM} (×10^{-3} A/m)
κ (×10^{-4} SI)
VGP Latitude (°N)
UPPER TRIASSIC
CARNIAN
LADINIAN
MIDDLE TRIASSIC
SAN CASSIANO FM.
WENGEN FM.
Car 1
HST
TST
LST
FSST
GRO 10
GRH 90
GRH 80
GRH 3
GRH 8
GRH 7
GRH 2
GRH 100
GRH 9
GRH 1
Celtites epolensis
Celtites sp.
Asklepioceras sp.
Frankites sp.
Lecanites glaucus
Frankites cf. apertus
cf. Frankites sp.
Orestites sp.
cf. Protrachyceras sp.
Celtites sp. A
Zestoceras lorigae
Daxatina sp. vel Tracchyceras sp.
Carnites sp.
vigens-densus
secatus-vigens
Maclearnoceras sp.
cf. Joannites sp.
Frankites apertus
Lobites ellipticus
237.579 ± 0.042 Ma
237.680 ± 0.047 Ma
Marmolada Conglomerates
Raw data
3 points average
GR4r
GR4n
GR3r
GR3n
GR2r
GR2n
GR1r
GR1n
0 m
100
200
300
400
500
0
100
200
300
400
500
-90
-60
-30
0
30
60
90
Carbonate breccia
Conglomerate
Sandstone
Marlstone
Sandy Marlstone
Pelite
Marly Limestone
Calcarenite
FSST = Falling Stage System Tract
LST = Lowstand System Tract
TST = Transgressive System Tract
HST = Highstand System Tract
Slump
Ash bed

Figure 2

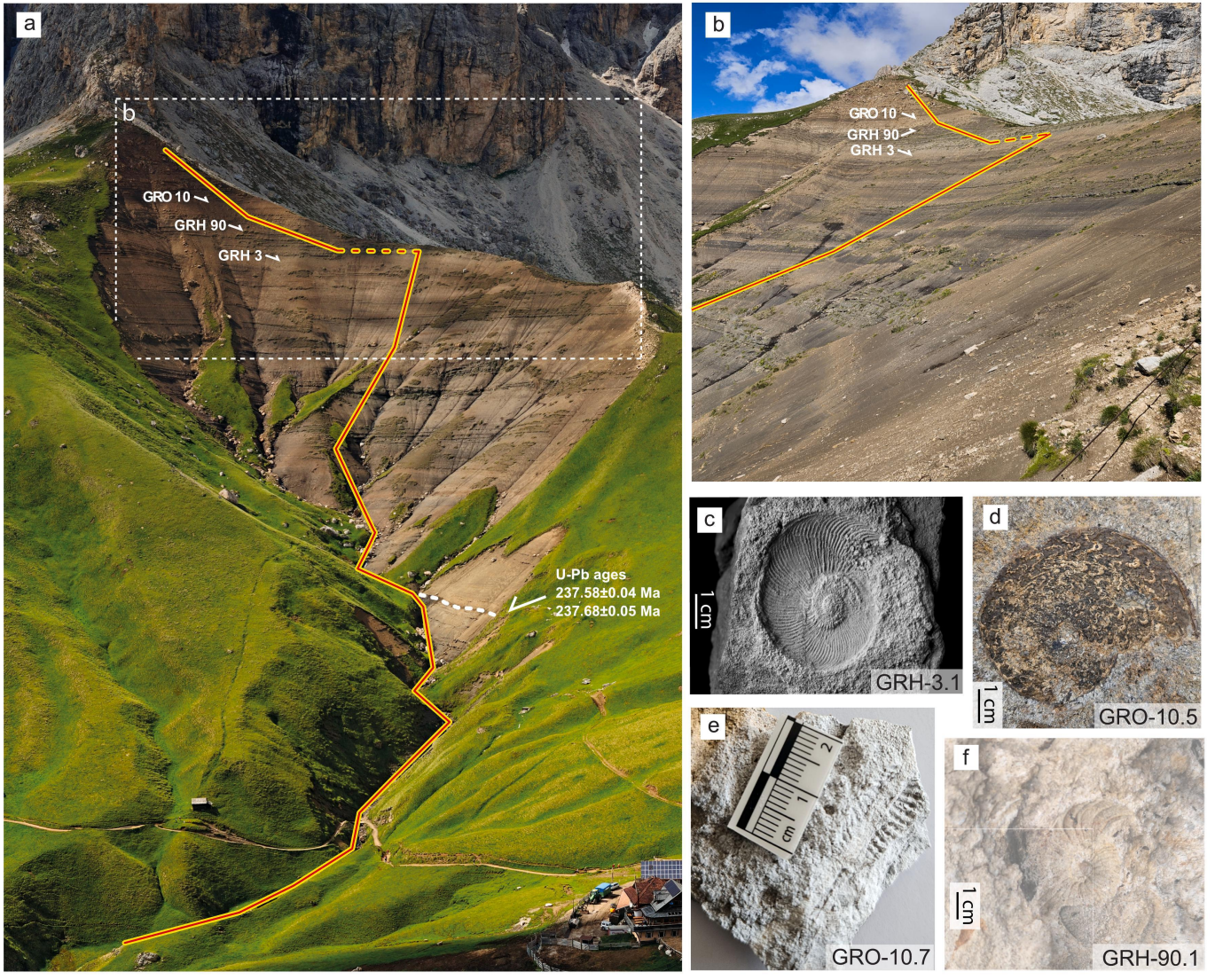
a
b
GRO 10
GRH 90
GRH 3
U-Pb ages
237.58±0.04 Ma
237.68±0.05 Ma
b
GRO 10
GRH 90
GRH 3
c
1 cm
GRH-3.1
d
1 cm
GRO-10.5
e
GRO-10.7
f
1 cm
GRH-90.1

Figure 3

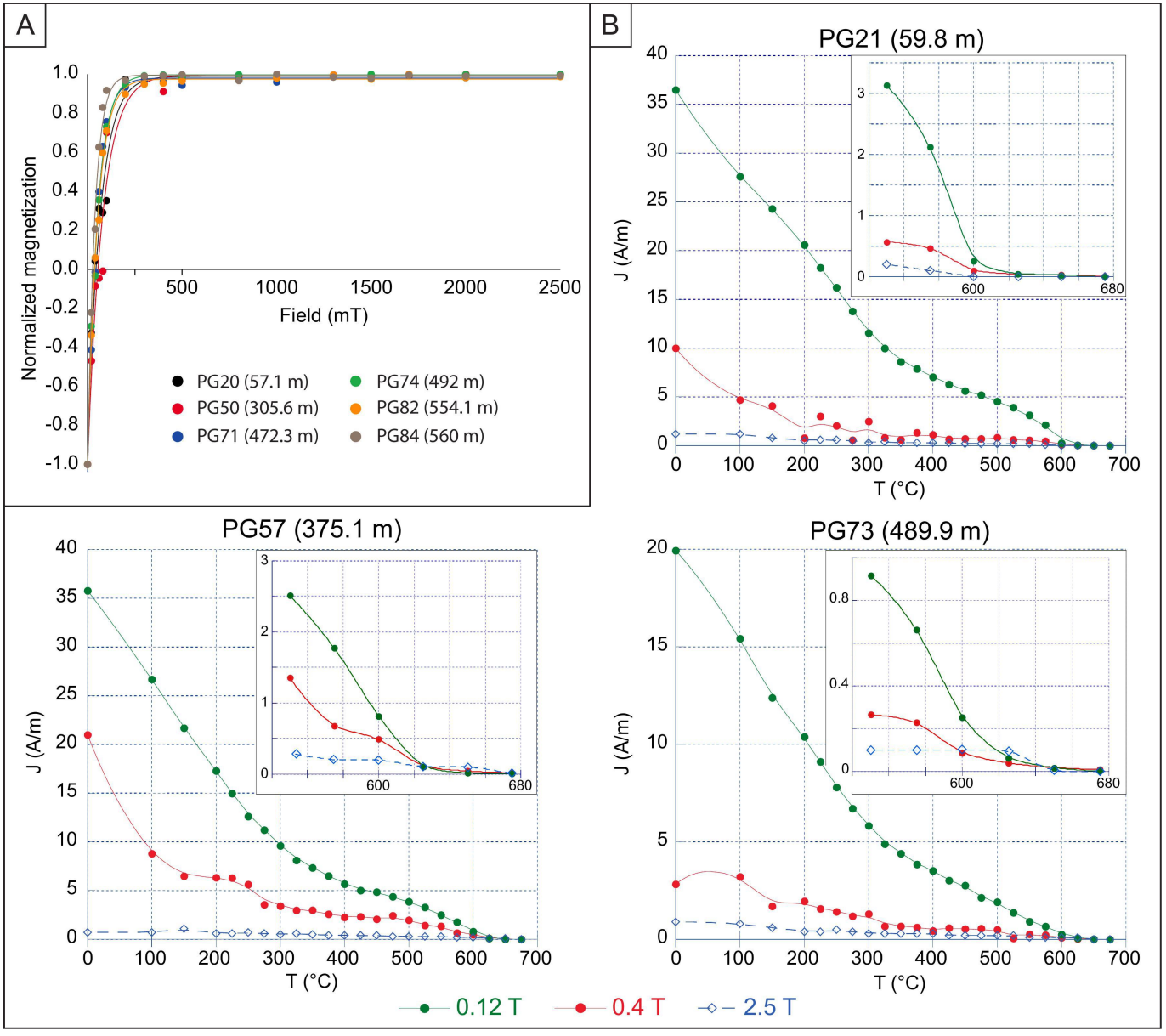
A
Normalized magnetization
Field (mT)
PG20 (57.1 m)
PG50 (305.6 m)
PG71 (472.3 m)
PG74 (492 m)
PG82 (554.1 m)
PG84 (560 m)
B
PG21 (59.8 m)
J (A/m)
T (°C)
PG57 (375.1 m)
PG73 (489.9 m)
0.12 T
0.4 T
2.5 T

Figure 4

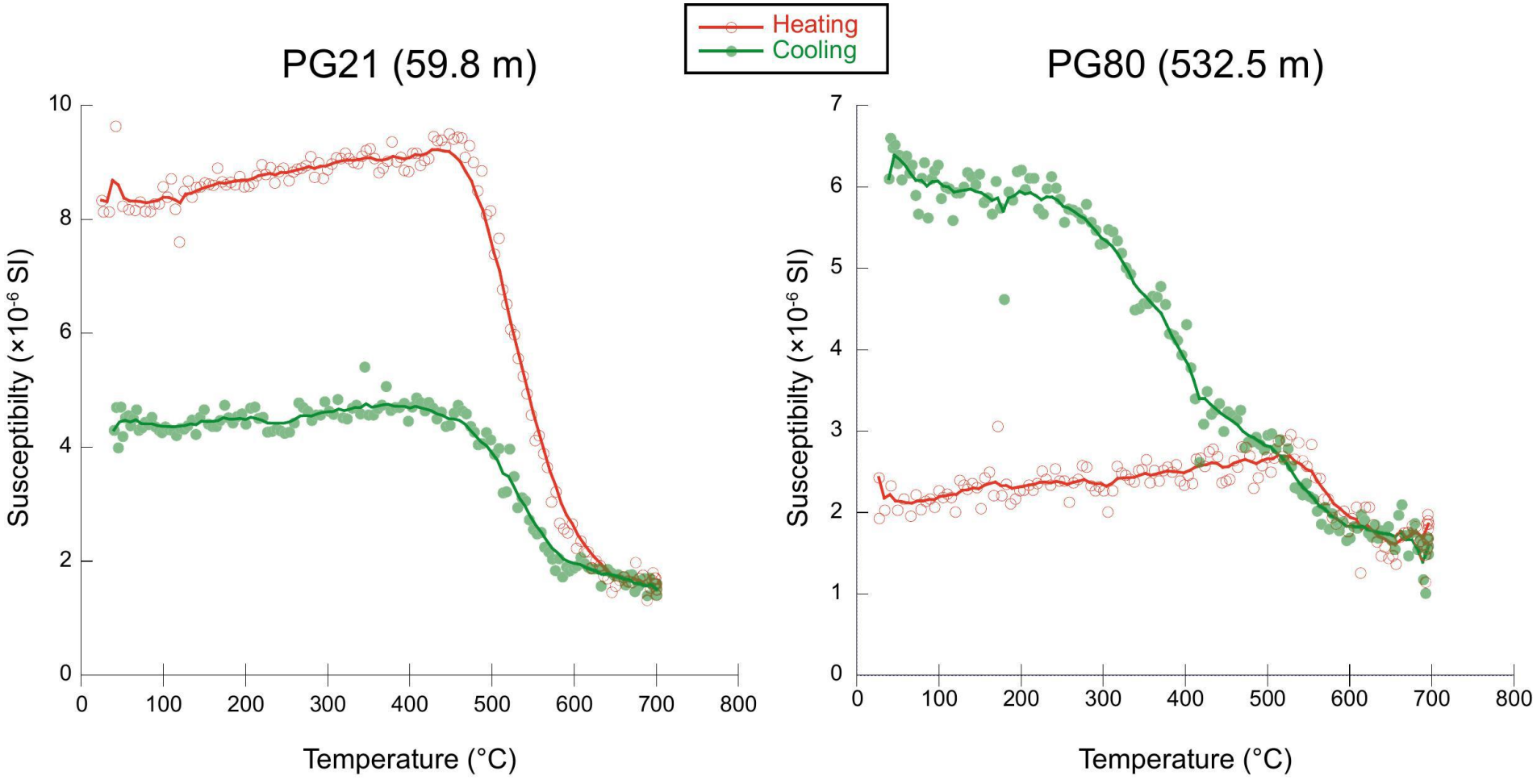
Heating
Cooling
PG21 (59.8 m)
PG80 (532.5 m)
Susceptibilty (×10-6 SI)
Temperature (°C)
0
100
200
300
400
500
600
700
800
1
2
3
4
5
6
7
8
10

Figure 5

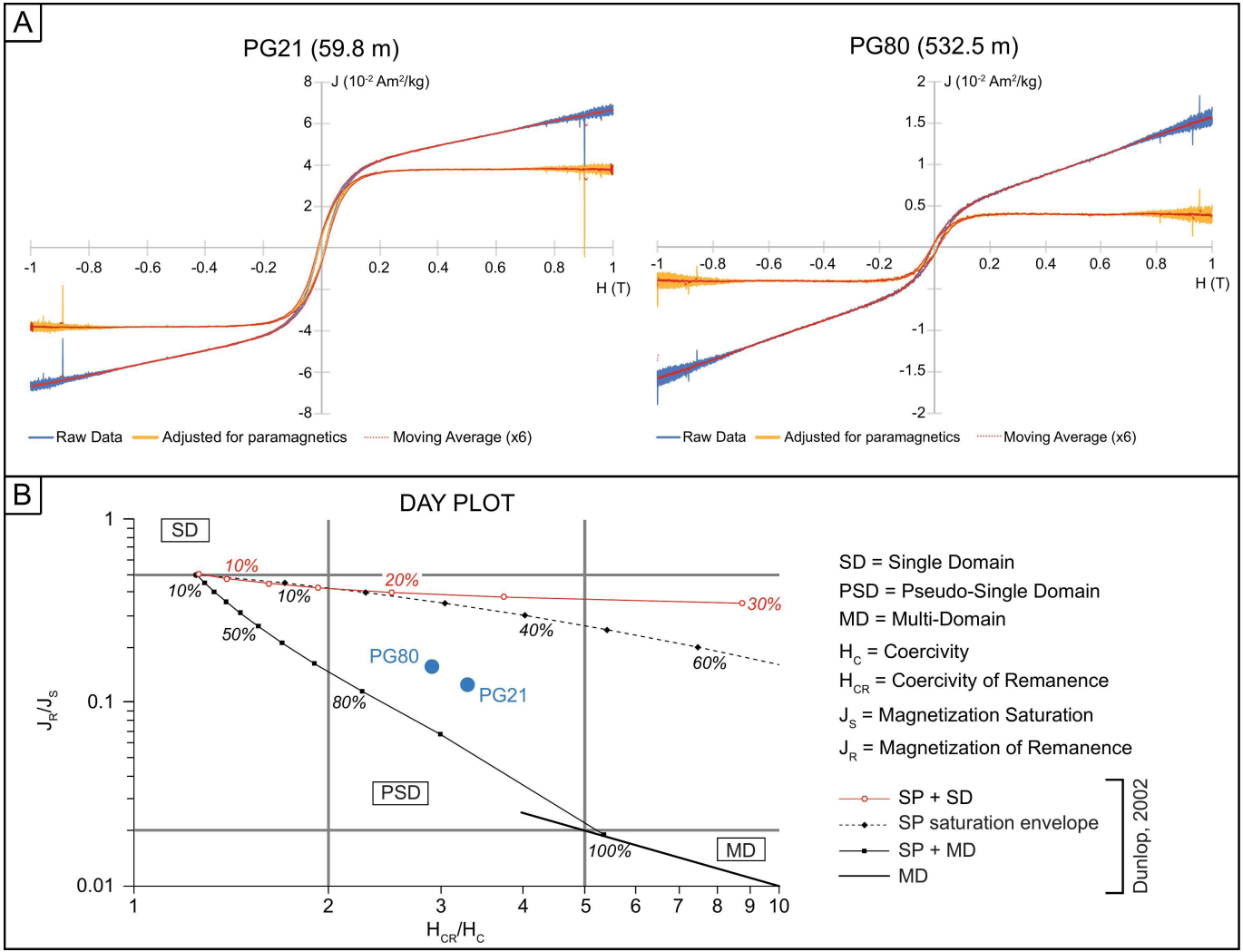
A
PG21 (59.8 m)
J (10-2 Am2/kg)
H (T)
Raw Data
Adjusted for paramagnetics
Moving Average (x6)
PG80 (532.5 m)
J (10-2 Am2/kg)
H (T)
Raw Data
Adjusted for paramagnetics
Moving Average (x6)
B
DAY PLOT
SD
PSD
MD
10%
20%
30%
40%
50%
60%
80%
100%
PG80
PG21
JR/JS
HCR/HC
SD = Single Domain
PSD = Pseudo-Single Domain
MD = Multi-Domain
HC = Coercivity
HCR = Coercivity of Remanence
JS = Magnetization Saturation
JR = Magnetization of Remanence
SP + SD
SP saturation envelope
SP + MD
MD
Dunlop, 2002

Figure 6

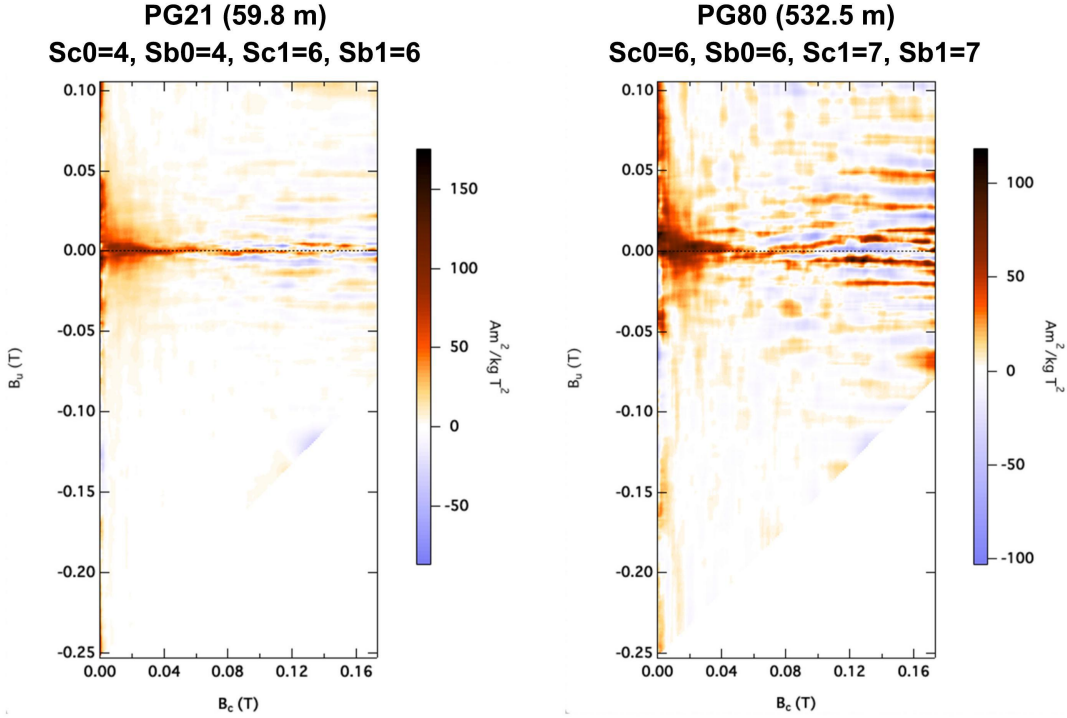
PG21 (59.8 m)
Sc0=4, Sb0=4, Sc1=6, Sb1=6
PG80 (532.5 m)
Sc0=6, Sb0=6, Sc1=7, Sb1=7
B_u (T)
B_c (T)
Am^2/kg T^2
0.10
0.05
0.00
-0.05
-0.10
-0.15
-0.20
-0.25
0.00
0.04
0.08
0.12
0.16
150
100
50
0
-50
-100

Figure 7

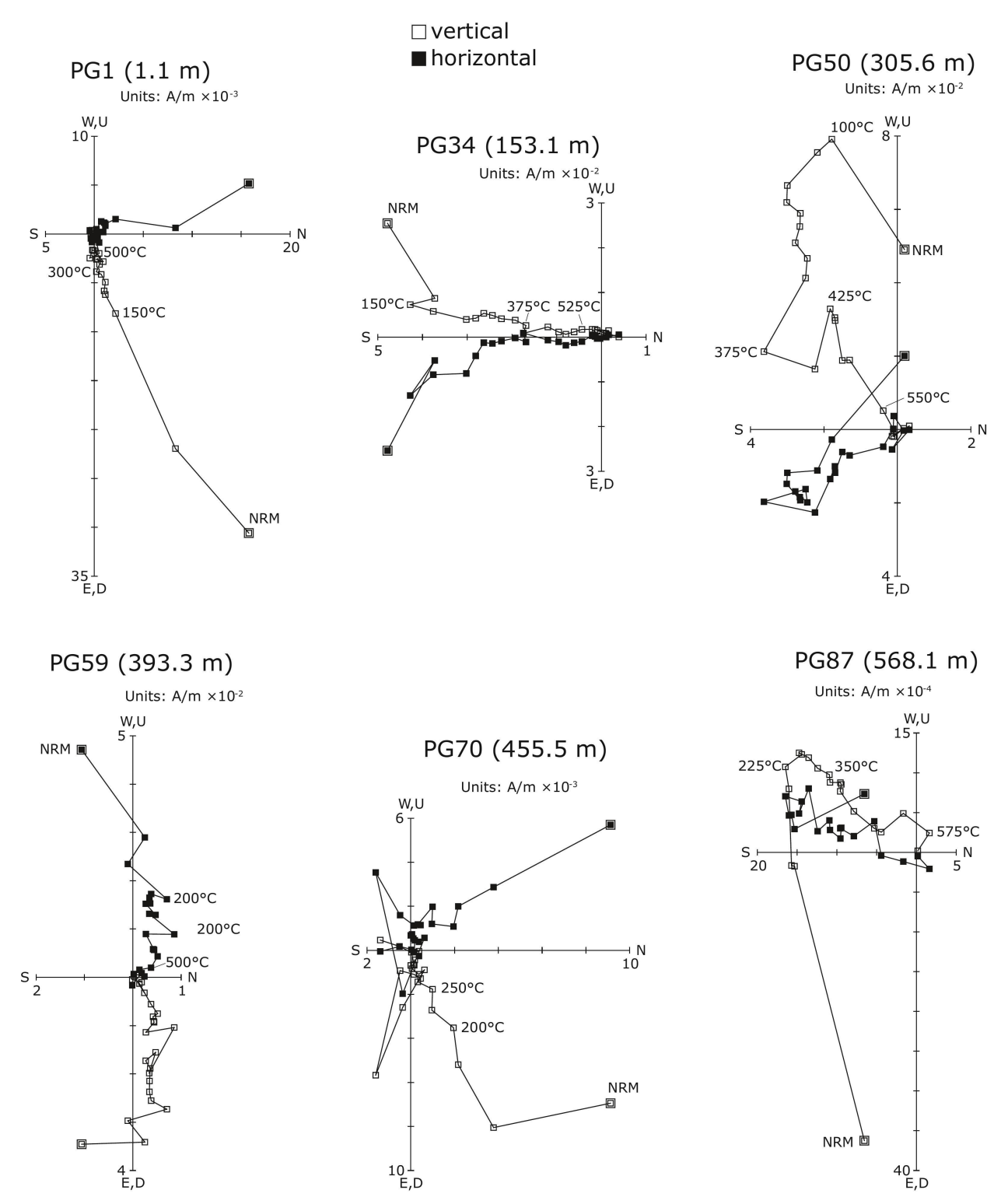
□ vertical
■ horizontal
PG1 (1.1 m)
Units: A/m ×10-3
W,U
10
S
5
N
20
500°C
300°C
150°C
NRM
35
E,D
PG34 (153.1 m)
Units: A/m ×10-2
W,U
3
NRM
150°C
375°C
525°C
S
5
N
1
3
E,D
PG50 (305.6 m)
Units: A/m ×10-2
100°C
W,U
8
NRM
425°C
375°C
550°C
S
4
N
2
4
E,D
PG59 (393.3 m)
Units: A/m ×10-2
W,U
5
NRM
200°C
200°C
500°C
S
2
N
1
4
E,D
PG70 (455.5 m)
Units: A/m ×10-3
W,U
6
S
2
N
10
250°C
200°C
NRM
10
E,D
PG87 (568.1 m)
Units: A/m ×10-4
W,U
15
225°C
350°C
575°C
S
20
N
5
NRM
40
E,D

Figure 8

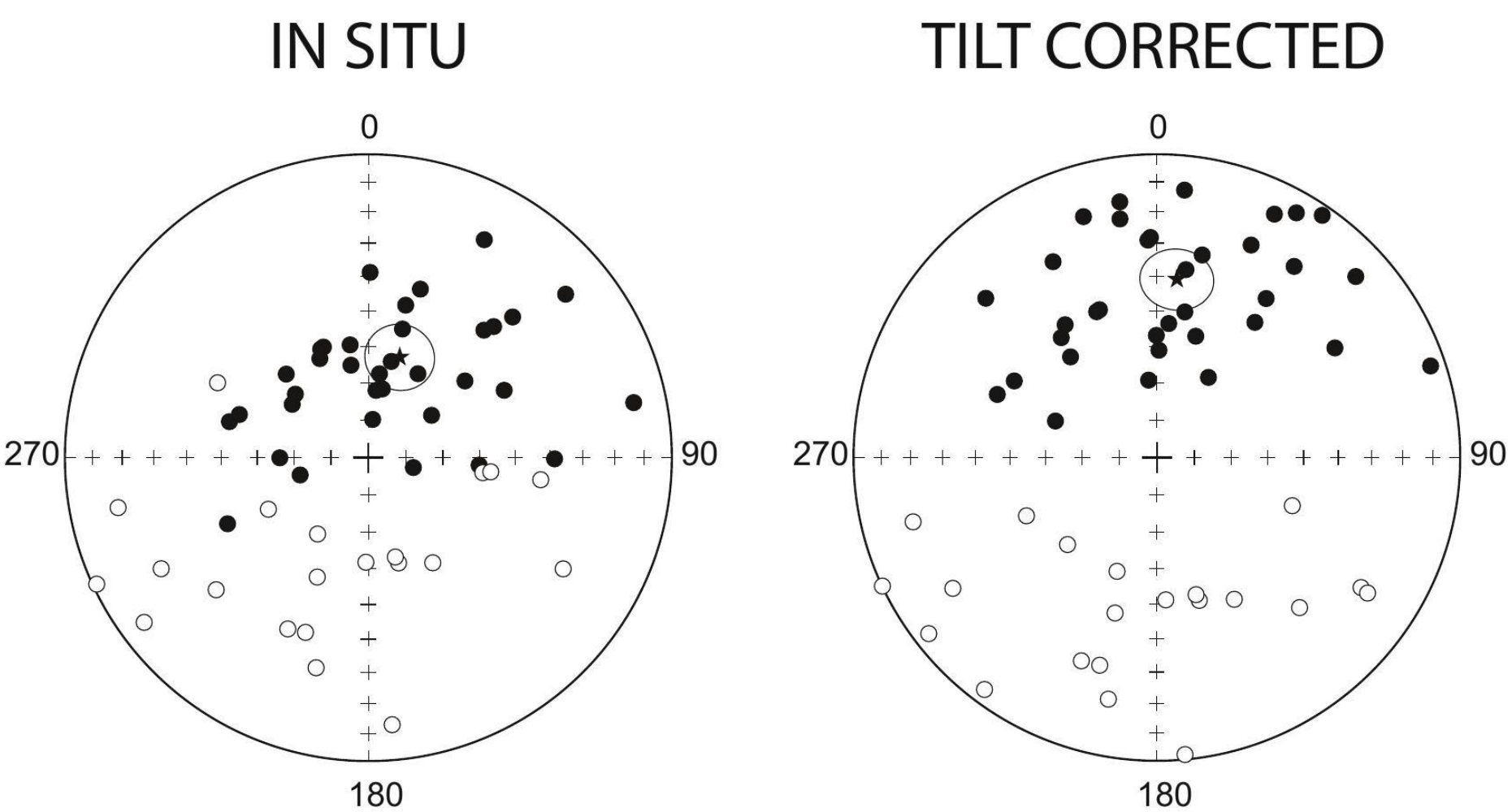

Figure 9

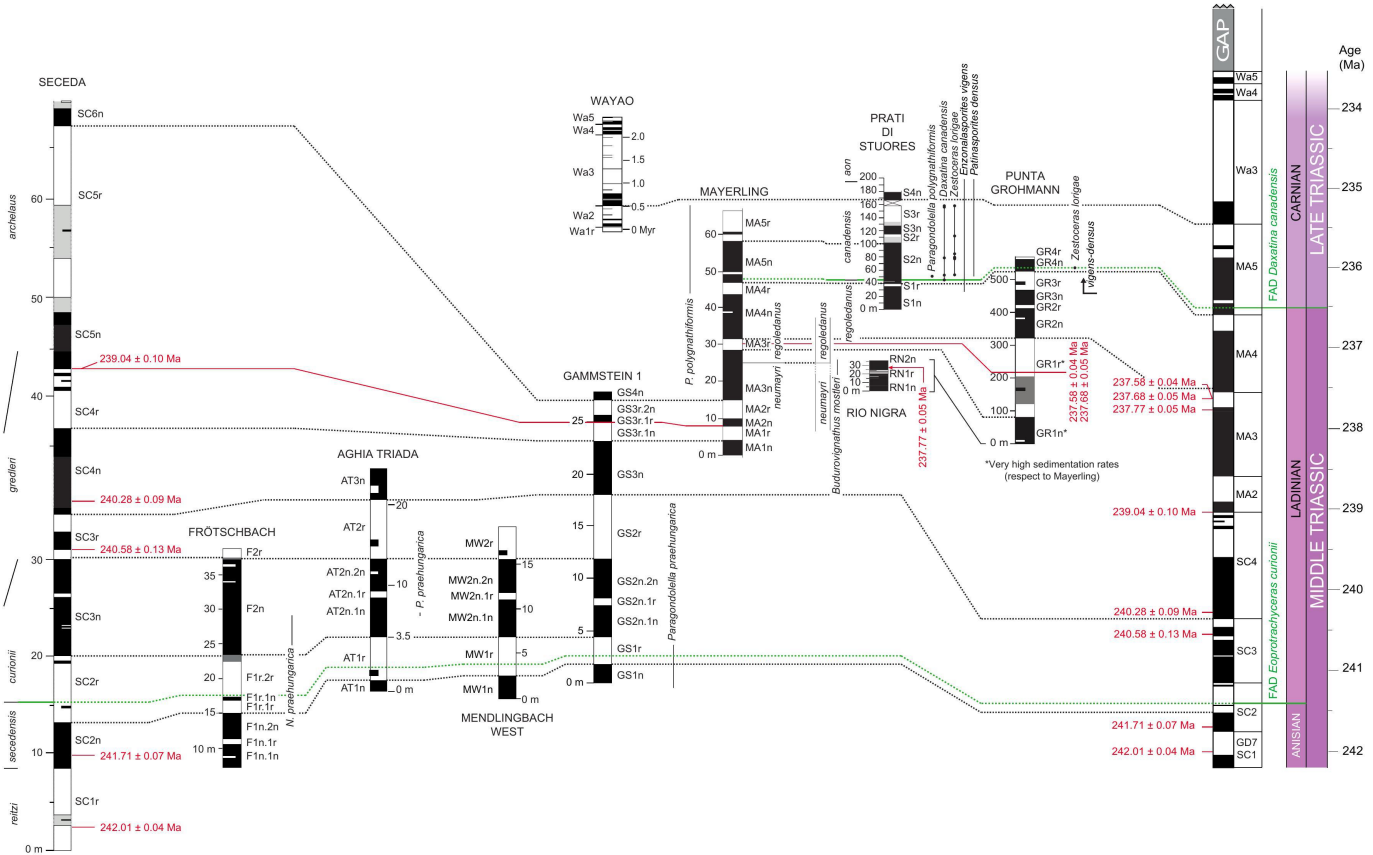
SECEDA
WAYAO
PRATI DI STUORES
MAYERLING
PUNTA GROHMANN
GAMMSTEIN 1
AGHIA TRIADA
FRÖTSCHBACH
MENDLINGBACH WEST
RIO NIGRA
GAP
Age (Ma)
CARNIAN
LADINIAN
ANISIAN
LATE TRIASSIC
MIDDLE TRIASSIC
FAD Daxatina canadensis
FAD Eoprodrachyceras curionii
239.04 ± 0.10 Ma
240.28 ± 0.09 Ma
240.58 ± 0.13 Ma
241.71 ± 0.07 Ma
242.01 ± 0.04 Ma
237.58 ± 0.04 Ma
237.68 ± 0.05 Ma
237.77 ± 0.05 Ma
*Very high sedimentation rates (respect to Mayerling)
archelaus
gradleri
curionii
secedensis
reitzi
P. polygnathiformis
Paragondolella praehungarica
Budurovignathus mosleri
neumayri
regoledanus
canadensis
aon
Paragondolella polygnathiformis
Daxatina canadensis
Zestoceras lorigae
Enzonalasporites vigens
Patinasporites densus
Zestoceras lorigae
vigens-densus
- P. praehungarica
N. praehungarica

Figure 10

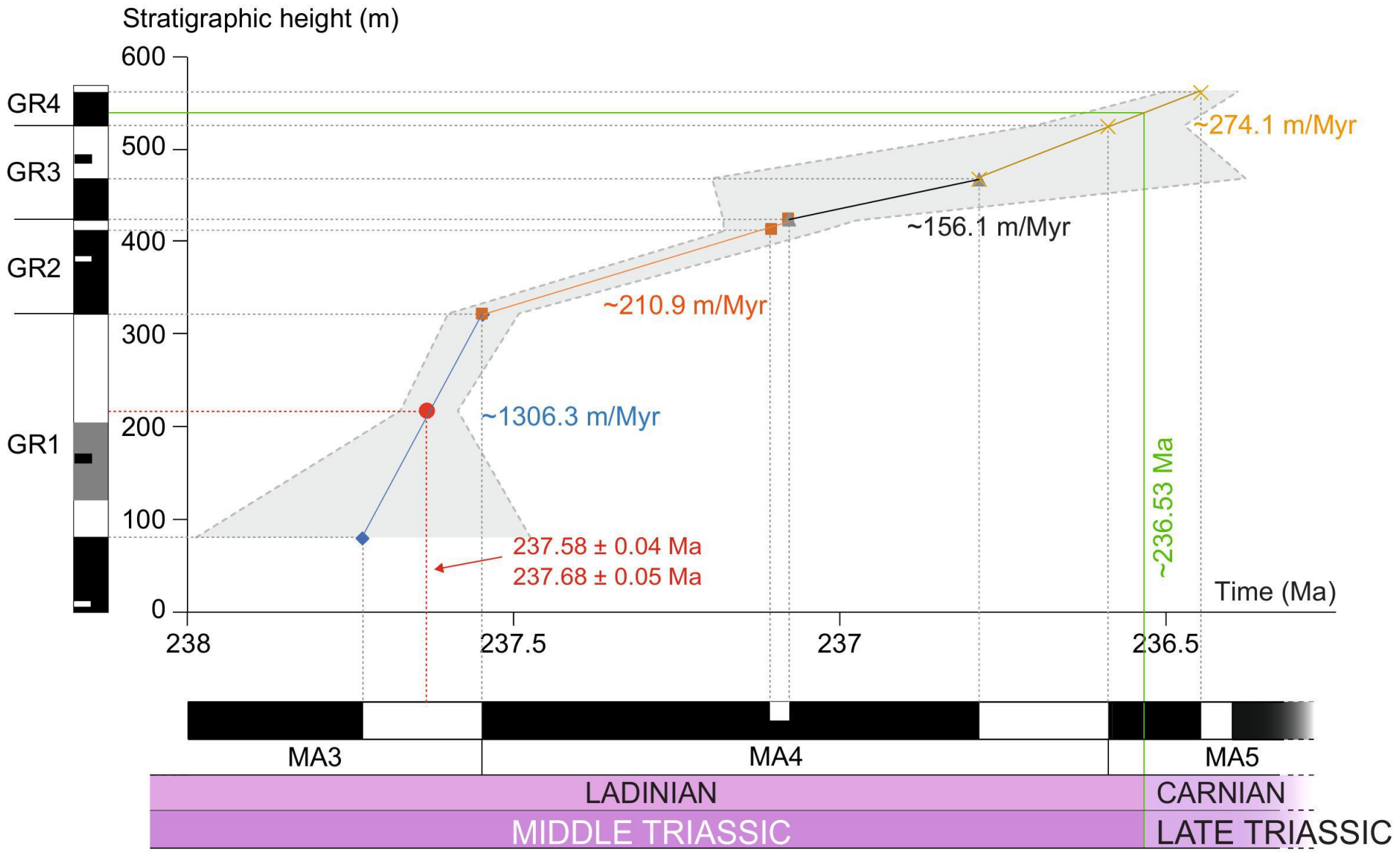
Stratigraphic height (m)
600
500
400
300
200
100
0
GR4
GR3
GR2
GR1
~274.1 m/Myr
~156.1 m/Myr
~210.9 m/Myr
~1306.3 m/Myr
237.58 ± 0.04 Ma
237.68 ± 0.05 Ma
~236.53 Ma
Time (Ma)
238
237.5
237
236.5
MA3
MA4
MA5
LADINIAN
CARNIAN
MIDDLE TRIASSIC
LATE TRIASSIC

Figure 11